AIAA 01–4318

Experimental and Computational Results for a Power-Law Elliptic-Section Projectile in a Supersonic Air-Stream

Paul H. Schuricht
John J. Bertin
James R. Forsythe
Michael L. Smith
U.S. Air Force Academy, CO 80840

Gregg L. Abate
Air Force Research Laboratory Munitions Directorate,
Eglin Air Force Base, FL 32542

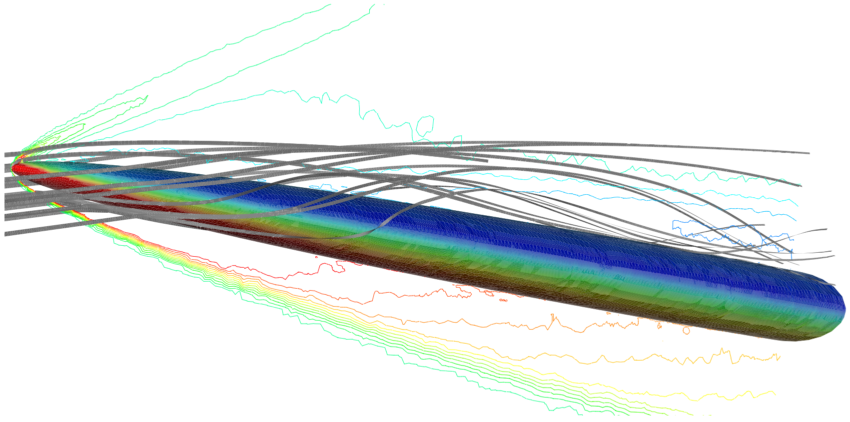

Atmospheric Flight Mechanics 2001
6–9 August 2001 / Montreal, Canada

For permission to copy or republish, contact the American Institute of Aeronautics and Astronautics
1801 Alexander Bell Drive, Suite 500, Reston, VA 20191–4344

Experimental and Computational Results for a Power-Law Elliptic-Section Projectile in a Supersonic Air-Stream

Paul H. Schuricht[*]
John J. Bertin[†]
James R. Forsythe[‡]
Michael L. Smith [§]
U.S. Air Force Academy, CO 80840
Gregg L. Abate[¶]
Air Force Research Laboratory Munitions Directorate, Eglin Air Force Base, FL 32542

Surface-pressure measurements and force-and-moment measurements have been obtained in experimental programs that have been conducted in the Tri-Sonic Wind-Tunnel (TWT) at the Aerodynamic Research Center (ARC) at the U.S. Air Force Academy (USAFA). Flow visualization data were obtained in the form of schlieren photographs and surface oil-flow patterns that were obtained during these test programs. Data were obtained at a Mach number of 4.28 over a range of Reynolds numbers (based on the free-stream conditions and the model length) of 12.47×10^6 to 19.96×10^6 over an angle-of-attack range from $-11°$ to $+11°$. The data from these wind-tunnel tests were compared with computations generated using the Cobalt$_{60}$ code, which was run on the Beowulf cluster at the High-Performance Computing Facility (HPCF) at the ARC. It should be noted that the experimental and the computational parts of this investigation were conducted concurrently in a double-blind fashion. That is, the results from the experimental effort were not used to influence the way in which the results from the CFD effort were produced and vice versa. The flow fields for slender (one-half) power-law elliptic section (PLES) configurations in a Mach 4.28 air-stream, as determined from the information generated through tests in the Tri-Sonic Wind Tunnel (TWT) and through the computations made using the Beowulf cluster are discussed in the present paper.

Introduction

MANEUVERABLE, high-energy projectiles that can be launched either from stationary guns or from mobile guns have the potential to enhance significantly the military effectiveness of the weapons system. Applications (both offensive and defensive) include air-to-air, air-to-surface, surface-to-air, and surface-to-surface scenarios. Non-conventional configurations offer the possibility of generating larger amounts of lift than would be produced by configurations with an axi-symmetric cross-section. Hence they are potentially more maneuverable. Examples of such non-conventional configurations are (one-half)-power-law elliptic-section (PLES) configurations. (One-half)-power-law elliptic-section configurations not only produce relatively large amounts of lift, but they are also more amenable to the blunting that is required to limit the severity of the aerodynamic heating to the vehicle surface in the vicinity of the stagnation point. Another advantage of elliptic-section bodies is the relatively small perturbation to the flow field when compared to those for conventional cone-cylinder-flare configurations. As a result, the design for launchability is made easier.

The United States Air Force Research Laboratory Munitions Directorate (AFRL/MNA) is part of an international effort to develop enhanced capabilities to predict the aerodynamics of future, advanced hypersonic systems, such as those described in the previous paragraph. The design process makes complementary use of experimental programs and of analytical/numerical methods of varying degree of rigor. Although the geometry for PLES configurations is relatively simple, the subsequent discussion will demonstrate that the flow fields contain subtle complexities. Thus, it is important that the wind-tunnel tests and the computational algorithms used in the design process properly model the flow physics.

Experimental data were obtained on right-elliptic

---

[*] Post-Doctoral Research Fellow, supported by the National Research Council/U.S. Air Force Academy DFAN Research Associateship, Member of AIAA

[†] Professor of Aeronautics, Fellow of AIAA

[‡] Assistant Professor, Member of AIAA

[§] Professor Emeritus, Consultant, Associate Fellow of AIAA

[¶] Aerospace Engineer, Senior Member of AIAA cones and on (one-half)-power-law elliptic-section cones in a Mach 8.2 air-stream in the Cranfield University Hypersonic Gun Tunnel.[1] Schlieren photographs were used to define the shape of the shock wave for the right-elliptic cone. Kontis et al.[1] noted: "The distance between the shock wave and the body, for 0°incidence, is greater in the meridian plane containing the minor axis than in the meridian containing the major axis. The shock wave is not an ellipse similar to the body, but is 'pushed in' toward the major axis and 'pulled out' from the minor axis. This shape is because of the presence of a cross flow from the high pressure sides at the ends of the major axis to the low pressure sides at the ends of the minor axis."

Oil-flow patterns that were obtained during the present program indicated that, even at relatively low angles-of-attack, boundary-layer separation occurred as the air flowed from the windward surface, around the relatively sharp change in cross section that occurs near the yaw plane. The free-vortex type of separation contained supersonic helical vortices that coalesced in the leeward plane-of-symmetry.[2] The recirculating, helical vortical flow impinged on the surface, creating an attachment line in the leeward plane-of-symmetry. The reattaching vortex pair produced a feather pattern in the oil film on the leeward surface of the model as the recirculating flow proceeded downstream and away from the leeward plane-of-symmetry. The oil-flow patterns obtained during the present program with the PLES model at an angle-of-attack of 10°indicated that a second, imbedded free-vortex-type separation occurred long before the recirculating flow reached the yaw plane. Thus, even for relatively small angles-of-attack, the flow field around the elliptic cross-section contained both primary and secondary separation streamlines.

Based on surface oil-flow patterns, Kontis et al.[1] also concluded that: "The flow separates on the leeward side of the body to form a pair of counter rotating vortices at low incidence for all models tested. The vortices grow with incidence"

An experimental program has been conducted by Pagan et al.[3] to develop an understanding of the vortical structures that form when boundary-layer separation occurs at moderate or high angles-of-attack. The experimental investigation of the flow field for an ogive cylinder at supersonic free-stream Mach numbers focused on the influences both of incidence and of turbulence. At low-to-moderate incidences (up to 10°), the flow structure included a primary cross-flow separation and a secondary cross-flow separation. As a result, the flow field contained both a primary and a secondary vortex. Pagan et al.[3] found that the influence of turbulence was strongest at low incidence.

For the conceptual design phase, reasonable estimates of the aerodynamic characteristics of the configuration may be made with aeroprediction codes that make considerable use of semempirical techniques[4] or of relatively simple analytical techniques.[5] The comments made in the previous paragraphs indicate that, even though the configuration geometry is fairly simple, the flow fields for PLES configurations contain some subtle complexities. Kontis et al.[6] noted: "in the conceptual design phase, a simple description of the aerodynamic characteristics is sufficient to assess candidate configurations. As the development process carries on, the complexity and detail required increases and the source of data changes, from an almost exclusive reliance on engineering prediction methods, to a high dependence on results from detailed wind tunnel tests. There are obvious advantages in being able to proceed further with weapons development before limitations of available prediction methods force the designer to resort to expensive and time consuming wind tunnel tests. In recent years an increasing number of new weapon designs have included features, such as non-circular cross-sectional bodies, air intakes, or novel control concepts, which cannot usually be addressed using engineering prediction methods."

Grasso and Iaccarino[7] state: "Numerical simulations may suffer from a lack of understanding of the controlling phenomena and/or inappropriate physical models, as well as limited experimental information." Grasso and Iaccarino[7] noted further that: "at high incidence and even for (geometrically simple) slender bodies, in the leeside region PNS results may show some differences with respect to the full Navier-Stokes results. We also recall that numerical simulations are strongly affected by the numerical methodology, i.e., the accuracy, efficiency, physical and geometrical modeling, etc. The use of computational fluid dynamics then poses the question of how one can be sure of the accuracy of the computed solution, i.e., how reliable a solution is for the understanding of physical phenomena or for the estimation of critical issues." The problems associated with the computation of these unique flowfields are only exacerbated when there is a lack of experimental data available to help interpret the computational results.

Shereda et al.[8] discussed force, moment, and surface-pressure data that were obtained for PLES configurations at angles-of-attack from $-4°$ to $+20°$ at Mach numbers from 1.5 to 5.0. Three models were built and tested, having ellipticity ratios of 2.0:1, 2.5:1, and 3.0:1. All three models were 36.0 inches long. Based on limited comparisons, the parameters computed using the Supersonic/Hypersonic Arbitrary Body Program (S/HABP) did not agree well with the corresponding measured values. However, Shereda et al.[8] concluded: "During this study a number of different types of analysis codes have been used to generate theoretical results for data/theory comparisons. Both of the Euler codes used in this study, FLO57 and NSWC, did a very good job of predicting the pressure distribution, normal force and pitching moment at angles of attack of 6 degrees or less. Since the Euler codes are inviscid the axial forces predicted do not include the viscous effects and the correct prediction of the axial force coefficient requires that the viscous effects be accounted for."

Shepherd and Tod[9] discussed selected force, moment, and surface-pressure data from those that were reported by Shereda et al.[8] Specifically, the data were for a PLES configuration having an ellipticity ratio of 2.5:1 at an angle-of-attack between 0° and 4° at Mach numbers of 2.0 and of 5.0. Shepherd and Tod[9] compared these data with flowfield computations that they had generated using a Multiblock Euler Flow Code. Agreement between computed and measured normal force coefficients was good at both Mach numbers for all angles-of-attack. However, Shepherd and Tod[9] concluded that the failure of the Euler Flow Code to model the boundary layer consistently led to under-prediction of the surface pressures, both on the windward and on the leeward surfaces.

Edwards and Roper[10] reported on a computational assessment of the static and of the dynamic coefficients for a PLES body at hypervelocity speeds, specifically, Mach 5 to Mach 9. Flow fields computed using CHASM, a parabolised Navier-Stokes (PNS) code, were compared with second-order shock-expansion (SOSE) and with Newtonian solutions that were generated using the DATCOM Code. The computational results were also compared against the experimental results that were obtained in the Cranfield University Gun Tunnel at Mach 8.2. The three computational methods not only correctly predicted the experimental trends, but were in generally good agreement with the experimental data. While the SOSE method proved best at predicting the drag coefficient, CHASM provided the better predictions for the lift coefficient, for the pitching-moment coefficient, and for the lift-to-drag ratio.

Surface-pressure measurement[11] and force-and-moment measurements[12] have been obtained in experimental programs that have been conducted in the Tri-Sonic Wind-Tunnel (TWT) at the Aerodynamic Research Center (ARC) at the U.S. Air Force Academy (USAFA). Flow visualization data were obtained in the form of schlieren photographs and surface oil-flow patterns that were obtained during these test programs. Data were obtained at a Mach number of 4.28 over a range of Reynolds numbers (based on the free-stream conditions and the model length) of 12.47×10^6 to 19.96×10^6 over an angle-of-attack range from $-11°$ to $+11°$. The data from these wind-tunnel tests were compared with computations generated using the Cobalt$_{60}$ code,[13] which was run on the Beowulf cluster at the High-Performance Computing Facility (HPCF) at the ARC. It should be noted that the experimental and the computational parts of this investigation were conducted concurrently in a double-blind fashion. That is, the results from the experimental effort were not used to influence the way in which the results from the CFD effort were produced and vice versa. The flow fields for slender (one-half) power-law elliptic section (PLES) configurations in a Mach 4.28 air-stream, as determined from the information generated through tests in the Tri-Sonic Wind Tunnel (TWT) and through the computations made using Cobalt$_{60}$ are discussed in the present paper.

Nomenclature

a	Major axis dimension (total width) at the base
b	Minor-axis dimension (total width) at the base
C_{Mo}	Pitching moment coefficient about the apex of the model, see eqn(6)
C_X	Axial force coefficient, see eqn (5)
C_Z	Normal force coefficient, see eqn (5)
L	Model length
L_{ref}	Reference length in the definition of the pitching-moment coefficient (= a, the dimension of the major axis at the base)
M_o	Pitching moment about the apex of the model
M_1	Free-stream Mach number
P	Static pressure
$P_{b,ave}$	Average value of the two measurements of the static pressure in the base region of the model
P_1	Free-stream static pressure
P_{t1}	Total pressure in the tunnel stagnation chamber, also Pt1
q_1	Free-stream dynamic pressure, $(\gamma/2)P_1M_1^2$
Re_L	Reynolds number, based on the free-stream conditions and the model length
S	Model base area, $\pi ab/4$
T_{t1}	Total temperature in the tunnel stagnation chamber
x	Axial coordinate, see Fig. 3
X	Axial force (parallel with the x-axis)
y	Transverse, or yaw-plane, coordinate, see Fig. 3
y_{max}	Maximum value of the y-coordinate at a given x-station
z	Vertical, or pitch-plane, coordinate, see Fig. 3
z_{max}	Maximum value of the z-coordinate at a given x-station
Z	Normal force (a positive normal force is in the negative z-direction)
γ	Ratio of specific heats, 1.4 for perfect air
ϕ	Roll angle, or model axial rotation, $\phi = 0°$ corresponds to the negative z side of the xz-plane; $\phi = 270°$ corresponds to the positive y side of the xy plane

Experimental Program

The Facility

The experimental investigation utilized the Tri-Sonic Wind Tunnel (TWT) of the Aeronautical Research Center (ARC). The TWT is a blow-down fa-

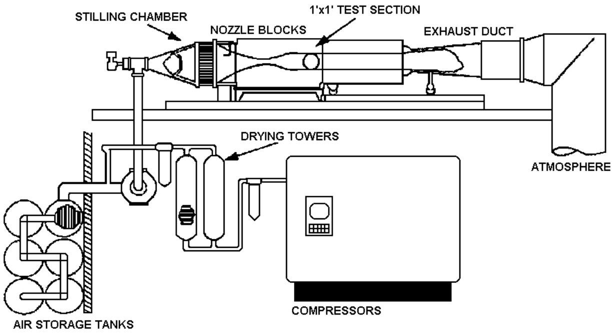

Fig. 1 Schematic of USAF Academy Tri-Sonic Wind Tunnel.

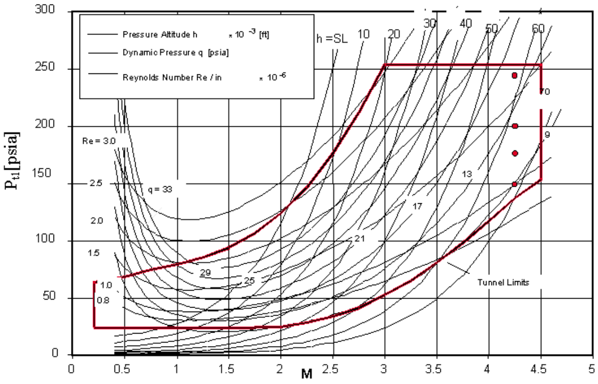

Fig. 2 Tri-Sonic Wind Tunnel performance envelope.

cility that discharges to the atmosphere, as shown in Fig. 1. For a run, the air passes from the holding tanks, through a series of control valves, into a stagnation (stilling) chamber, through a convergent/divergent nozzle, and into the test section, which is 1-foot by 1-foot square. The total pressure in the stagnation chamber (P_{t1}) is sensed by a transducer having a full-scale range of 300 psia with a combined nonlinearity and hysterises of ±0.3% full scale. The maximum total pressure in the stagnation chamber, which occurs at the higher Mach numbers (see Fig. 2), is 250 psia. The total temperature in the stagnation chamber is sensed by a Type E (chromel/constantan) thermocouple capable of measuring $-328°F$ to $1652°F$ with a sensitivity of $37.7 \pm V/°F$. The total temperature can be varied only slightly, being $560°R \pm 20°R$.

Fixed nozzle blocks form the convergent/divergent nozzle through which the air accelerates from the stagnation chamber into the test section. By selecting from the nozzle blocks that are available one can provide test section Mach numbers at specific, selected design values in the range of 0.14 to 4.50. As shown in Fig. 2, the operating range of total pressure in the tunnel reservoir (P_{t1}) is a function of the test-section Mach number. By varying the pressure in the stagnation chamber of the TWT, one can control the unit free-stream Reynolds number in the test section. Depending upon the test-section Mach number, it is possible to generate free-stream unit Reynolds numbers from approximately 6×10^6 per foot to approximately 36×10^6 per foot.

The run time is a function of the total temperature (T_{t1}), the total pressure in the tunnel reservoir (P_{t1}), and the nozzle throat area (which, since the cross-section area of the test section is fixed, relates uniquely to the Mach number in the test section). Usable run times range from 20 seconds to 420 seconds.

The Test Conditions

For the nozzle blocks that were used in the present program, the free-stream Mach number in the test section was 4.28 ± 0.04, which was determined from a facility calibration program. The total temperature was assumed to be constant at a value of $T_{t1} = 560°R$. Pressure measurements were obtained at stagnation pressures of approximately 150 psia, 175 psia, 200 psia, and 240 psia. Since the total temperature and the test-section Mach number are constants, the Reynolds number is directly proportional to the stagnation pressure. Thus, the corresponding Reynolds numbers, based on the free-stream conditions and on the model length are presented in Table 1.

Table 1 Correlation between the stagnation chamber pressure and the free-stream Reynolds number based on model length of 12.00 inches for the nominal test conditions of the present program

P_{t1} (psia)	$Re_L \times 10^{-6}$ (-)
150	11.74
175	13.69
200	15.65
240	18.79

Measurements of the forces, of the moments, and of the surface pressures were obtained at angles-of-attack of ±11°, ±10°, ±8°, ±6°, ±4°, ±2°, and 0° for all four Reynolds numbers.

The Models

A computer-generated image of the baseline PLES configuration showing the coordinate system is presented in Fig. 3. The origin of the coordinate system is at the apex of the model, with the x-axis corresponding to the longitudinal axis of the configuration. In accordance with the right-hand rule, the y-axis is positive to the left, when viewed from the rear of the model, and the z-axis is downward. The xy plane contains the major axis, while the xz plane contains the minor axis. The equations for the one-half power-law elliptic-section (PLES) configurations are

$$z = C_1 x^{0.5} \tag{1}$$

$$y = C_2 x^{0.5} \tag{2}$$

Fig. 3 Configuration geometry and coordinate system for slender, power-law elliptic-section model.

where the factors C_1 and C_2 define the thickness ratio of the model and the eccentricity of the elliptic cross section. For this report, the units for the physical coordinates (x, y, and z) in these two equations are inches. The lines traced out by these equations are connected by ellipses of eccentricity 5/3 centered on the x-axis. Thus,

$$C_2 = \left(\frac{5}{3}\right) C_1 \tag{3}$$

and

$$a = \left(\frac{5}{3}\right) b \tag{4}$$

The model geometries will be defined by a three-letter code. The first letter will be used to identify, whether the model was built at the Eglin Air Force Base (E) or at the U.S. Air Force Academy (A). The second letter will identify whether the model is a force-and-moment model (F) or a pressure model (P). The third letter will identify the thickness ratio of the model, which is defined by the magnitude of the parameters C_1 and C_2 (or a and b). For the baseline models, which are designated by the symbol B, $C_1 = 0.119$ and $C_2 = 0.198$. A pair of models (both a P and an F) were built at the U.S. Air Force Academy to study the effect of the thickness ratio on the comparison between the measured parameters with those from the computed flow fields. The modified models have a thickness ratio that is 4/3 that for the baseline models and are designated by the symbol M, $C_1 = 0.159$ and $C_2 = 0.264$.

The reader should note that, for the models that were built at the Eglin Air Force Base, $L = 12.75$ inches. For the models that were built at the U. S. Air Force Academy, $L = 12.00$ inches. The Eglin model corresponds to the "H3" configuration. The 12.00 inch baseline Academy model is the H3 model with the final 0.75 inches removed, in order to fit the entire model into the calibrated portion of the test section. For the pressure measurements these two models are equivalent, since all pressure measurements were taken well forward of 12.00 inches. For the force and moment measurements, the models are not equivalent.

Fig. 4 The models tested, from left to right APM, APB, EPB

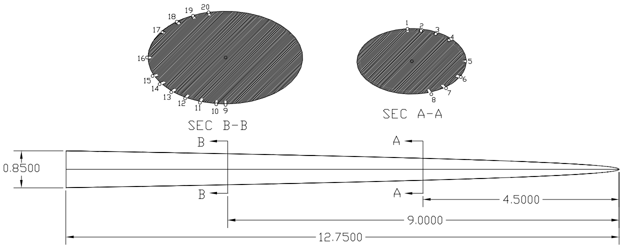

Fig. 5 Location of the surface pressure ports for the APB and EPB models

Presented in Fig. 4 and in Table 2 is a summary of the nomenclature and of the dimensions of the models for which data relevant to the present report were obtained.

Table 2 The nomenclature and the dimensions of the models for which data relevant to the present report were obtained

	L (*in.*)	$a(=L_{ref})$ (*in.*)	b (*in.*)	S (*in.*^{2})
EPB	12.75	1.417	0.850	0.946
APB	12.00	1.372	0.824	0.888
EFB[1]	12.75	1.417	0.850	0.946
AFB	12.00	1.372	0.824	0.888
APM	12.00	1.829	1.102	1.582
AFM	12.00	1.829	1.102	1.582

For the EPB and for the APB models, twenty orifices, flush-mounted in the model's surface, were used to sense static pressures acting on the model during a run. Although the "E" and the "A" models were of different length L, the pressure orifices were located in one of two planes that were the same distance from the apex regardless of the length of the model, i.e.,

---

[1] Force-and-moment data for the EFB model were obtained in the DREV TriSonic Wind Tunnel[14]

Table 3 Locations of the static pressure orifices for the EPB and APB models.

Port	x (in.)	x/L	y (in.)	y/ymax	z (in.)	z/zmax
1	4.5	0.353	-0.033	-0.080	-0.249	-1.000
2	4.5	0.353	+0.072	+0.175	-0.234	-0.922
3	4.5	0.353	+0.184	+0.448	-0.210	-0.793
4	4.5	0.353	+0.284	+0.691	-0.161	-0.562
5	4.5	0.353	+0.411	+1.000	0.000	0.000
6	4.5	0.353	+0.376	+0.915	+0.121	+0.478
7	4.5	0.353	+0.263	+0.640	+0.207	+0.818
8	4.5	0.353	+0.150	+0.365	+0.253	+1.000
9	9.0	0.706	-0.130	-0.216	+0.364	1.000
10	9.0	0.706	-0.250	-0.415	+0.360	+0.989
11	9.0	0.706	-0.375	-0.622	+0.347	+0.953
12	9.0	0.706	-0.484	-0.803	+0.315	+0.865
13	9.0	0.706	-0.603	-1.000	+0.266	+0.731
14	9.0	0.706	-0.560	-0.929	+0.205	+0.563
15	9.0	0.706	-0.506	-0.839	+0.142	+0.390
16	9.0	0.706	-0.417	-0.692	0.000	0.000
17	9.0	0.706	-0.311	-0.516	-0.195	-0.562
18	9.0	0.706	-0.196	-0.325	-0.275	-0.793
19	9.0	0.706	-0.071	-0.118	-0.320	-0.922
20	9.0	0.706	0.000	0.000	-0.347	-1.000

$x = 4.50$ inches and $x = 9.00$ inches. The locations of the pressure orifices are presented in Fig. 5 and in Table 3. Eight orifices were located in a cross-section plane that was nominally 4.50 inches from the apex of the model. Twelve orifices were located in a cross-section plane that was nominally 9.00 inches from the model apex. In this paper, spanwise pressure distributions at a station will be presented as a function of the dimensionless distance from the pitch plane, i.e., y/y_{max}, where y_{max} is the maximum value of y for that station. The orifices in the $x = 4.50$ inches plane are all meant to be located on the port side of the model, i.e., at positive values of y. Conversely, the orifices in the $x = 9.00$-inches plane are all meant to be located on the starboard side of the model, i.e., at negative values of y. This was done to simplify installing the hypodermic tubing in the model. However, model construction techniques resulted in the actual locations of the pressure orifices being slightly different than the specified locations. This can be seen in the pressure-orifice locations presented in Table 3 for the EPB model. Orifice no. 1, which was in the $x = 4.50$-inches plane, had a small negative y-coordinate.

A similar philosophy was used for locating the orifices to provide surface-pressure data for the APM model. However, because the APM model had a greater thickness ratio, it could accommodate 22 orifices, eleven at $x = 4.50$ inches and eleven more at $x = 9.00$ inches. The locations of the pressure orifices of the APM model are presented in Fig. 6 and in Table 4.

Table 4 Locations of the static pressure orifices for APM model.

Port	x (in.)	x/L	y (in.)	y/ymax	z (in.)	z/zmax
1	4.5	0.353	0.000	0.0	-0.337	-1.000
2	4.5	0.353	0.112	0.2	-0.301	-0.894
3	4.5	0.353	0.224	0.4	-0.261	-0.775
4	4.5	0.353	0.336	0.6	-0.213	-0.632
5	4.5	0.353	0.448	0.8	-0.150	-0.447
6	4.5	0.353	0.560	1.0	0.000	0.000
7	4.5	0.353	0.504	0.9	0.106	0.316
8	4.5	0.353	0.392	0.7	0.184	0.548
9	4.5	0.353	0.280	0.5	0.238	0.707
10	4.5	0.353	0.168	0.3	0.281	0.837
11	4.5	0.353	0.056	0.1	0.319	0.949
12	9.0	0.706	0.000	0.0	0.476	1.000
13	9.0	0.706	-0.158	-0.2	0.426	0.894
14	9.0	0.706	-0.317	-0.4	0.369	0.775
15	9.0	0.706	-0.475	-0.6	0.301	0.632
16	9.0	0.706	-0.634	-0.8	0.213	0.447
17	9.0	0.706	-0.792	-1.0	0.000	0.000
18	9.0	0.706	-0.713	-0.9	-0.150	-0.316
19	9.0	0.706	-0.554	-0.7	-0.261	-0.548
20	9.0	0.706	-0.396	-0.5	-0.337	-0.707
21	9.0	0.706	-0.238	-0.3	-0.242	-0.837
22	9.0	0.706	-0.079	-0.1	-0.451	-0.949

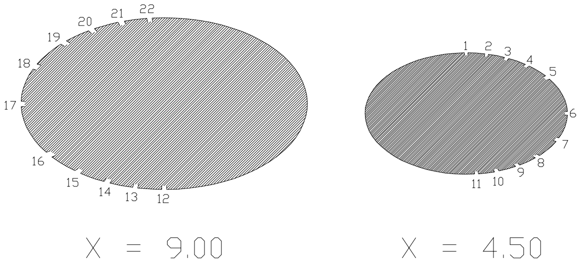

Fig. 6 Location of the surface pressure ports for the APM model

Note that the pressure measurements from those orifices on the top of the vehicle, i.e., those having negative z-coordinates, are on the leeward surface when the model is at a positive angle-of-attack. Furthermore, the pressure measurements from those orifices on the bottom of the vehicle, i.e., those having positive z-coordinates, are on the leeward surface, when the model is at a negative angle-of-attack. Thus, one can combine the data from two stops on the alpha sweep (combining the pressure measurements from the orifices having a negative z-coordinate for a specific, positive alpha with the pressure measurements from the orifices having a positive z-coordinate that were obtained at an alpha of the same magnitude, but negative in sign) to produce a composite, spanwise pressure distribution for the leeward surface. A similar approach would yield a detailed spanwise pressure distribution for the windward surface. This procedure requires that the symmetry of the model, the symmetry of the flow, and the run-to-run variations of the pressure measurements must be within acceptable limits. Data indicating that these three requirements were met will be presented in the section: "Results and Discussion".

For the models built at the U.S. Air Force Academy, the process was to build and test the "F" model first. Once the force-and-moment data had been obtained, the model was returned to the shop and the pressure tubing was placed in the model. Thus, the dimensions of the force-and-moment model were identical to those for the pressure model.

The measurements of the forces and of the moments were made using a six-component balance flush-mounted to the base of the model. The force coefficients (C_F), both for the axial force (X) and for the normal force (Z), were calculated using the relation that:

$$C_F = \frac{F}{q_1 S} \tag{5}$$

The coefficient for the pitching moment about the apex of the model, i.e., about $x = 0$, (C_{Mo}) was calculated using the relation that:

$$C_{Mo} = \frac{M_o}{q_1 S L_{ref}} \tag{6}$$

After mounting the model on the sting, two pressure probes were mounted on the sting. These probes were located on either side of the sting, approximately in-line with the yaw plane of the model and close to the base of the model. During the test runs, these probes sensed the static pressures in the base region. The two measurements were averaged to find the mean base pressure ($P_{b,ave}$), which was used in calculating the effective axial force (X_{eff}) and the effective axial-force coefficient ($C_{X,eff}$), as will be discussed later in the Results and Discussion Section. When mounting the PLES models in the test section, great care was taken to ensure that the model was correctly aligned with the axis of the wind tunnel. However, small offsets ($\pm 0.2^\circ$) were unavoidable. Before the testing began and at regular intervals during each series of runs, the model offset angle was measured. The offset angle was then added to the sting angle to provide the actual angle-of-attack that was used in the analysis of the data.

Comments Regarding Uncertainty and Repeatability

Uncertainty analyses were accomplished for both force and moment, and pressure data sets generated in the experimental program. The force and moment data were obtained from the output of the force balance in the wind tunnel, and the pressure data were obtained from the output of the scani-valve transducer. In both cases, the uncertainty is composed of two parts: the bias errors of the instrumentation and the precision errors of the measurements themselves. Bias errors are assumed to be consistent and repeatable, and are obtained from calibration data provided by the instrumentation manufacturer or from calibrations conducted in the test facility prior to the experimental program. Precision errors are assumed to be random and to conform to a normal distribution about a mean. By combining the two errors in an appropriate way, the overall uncertainty in the data can be obtained and, in this report, the uncertainties can be used to assess the statistical significance of the agreement or disagreement between experimental data and results obtained from CFD.

Force and Moment Uncertainty

The force and moment data are presented in the form of axial and normal force coefficients and the pitching moment coefficient referenced to the apex of the model. These coefficients must be expressed as functions of measured variables since it is the uncertainty in these variables that produces the uncertainty in the respective coefficients. Thus, using eqs. 5 and 6 as the starting point, the following results are obtained:

$$\begin{aligned} C_X &= \frac{X}{q_1 S} = \frac{X}{\frac{1}{2}\gamma P_1 M_1^2 S} \\ &= \frac{2X}{\gamma P_{t1} M_1^2 S}\left(1 + \frac{\gamma - 1}{2} M_1^2\right)^{\frac{\gamma}{\gamma - 1}} \end{aligned} \tag{7}$$

$$\begin{aligned} C_Z &= \frac{Z}{q_1 S} = \frac{Z}{\frac{1}{2}\gamma P_1 M_1^2 S} \\ &= \frac{2Z}{\gamma P_{t1} M_1^2 S}\left(1 + \frac{\gamma - 1}{2} M_1^2\right)^{\frac{\gamma}{\gamma - 1}} \end{aligned} \tag{8}$$

$$\begin{aligned} C_{Mo} &= \frac{M_o}{q_1 S L_{ref}} = \frac{M_o}{\frac{1}{2}\gamma P_1 M_1^2 S L_{ref}} \\ &= \frac{2}{\gamma P_{t1} M_1^2 S L_{ref}}\left(1 + \frac{\gamma - 1}{2} M_1^2\right)^{\frac{\gamma}{\gamma - 1}} \\ &\quad [N_1 x_1 - N_2 x_2 + (N_1 + N_2) x_{shift} - X z_{shift}] \end{aligned} \tag{9}$$

We note that the axial force coefficient is a function of the axial force X, the stagnation pressure P_{t1}, the free-stream Mach number M_1, and the reference (base) area S of the model. We assume the ratio of specific heats is constant at 1.4 with no uncertainty. Similarly, the normal force coefficient is a function of the same variables with the exception that the normal force replaces the axial force. The more complex expression for the pitching moment coefficient referenced to the apex of the model shows that it is a function of the two normal force component outputs (N_1 and N_2) of the force balance, the axial force X, the stagnation pressure P_{t1}, the free-stream Mach number M_1, the reference area of the model S, the reference moment arm L_{ref}, and the four lengths x_1, x_2, x_{shift}, and z_{shift} associated with the force balance.

As noted above, the uncertainty in each of these coefficients is determined by combining the bias and precision errors of each of the independent variables associated with each coefficient.

Using the axial force coefficient to illustrate, we seek to determine its bias and precision errors and combine them to find the uncertainty. The bias error, $\mathcal{B}_{C_X}$ is the root sum square of the weighted bias errors due to each of the independent variables that determine the axial force coefficient (see eq. 7). Thus:

$$\begin{aligned}\mathcal{B}_{C_X} &= \left[\left(\frac{\partial C_X}{\partial X}\mathcal{B}_X\right)^2 + \left(\frac{\partial C_X}{\partial P_{t1}}\mathcal{B}_{P_{t1}}\right)^2\right. \qquad (10)\\ &\quad \left. + \left(\frac{\partial C_X}{\partial M_1}\mathcal{B}_{M_1}\right)^2 + \left(\frac{\partial C_X}{\partial S}\mathcal{B}_S\right)^2\right]^{\frac{1}{2}}\end{aligned}$$

In this expression, the $\mathcal{B}$ symbols represent the bias errors of the respective variables represented by the subscripts. These errors are derived from calibrations of the instrumentation used to obtain the data.

The second source of uncertainty is the precision error. A measured variable must be recorded a sufficient number of times such that the normal distribution can be assumed to apply to the random variations in the measurements. The precision error is then calculated to a 95% confidence level as twice the standard deviation of that variable. The root sum square of the weighted precision errors associated with each contributing independent variable is then the precision error for the coefficient. Thus:

$$\begin{aligned}\mathcal{P}_{C_X} &= \left[\left(\frac{\partial C_X}{\partial X}\mathcal{P}_X\right)^2 + \left(\frac{\partial C_X}{\partial P_{t1}}\mathcal{P}_{P_{t1}}\right)^2\right. \qquad (11)\\ &\quad \left. + \left(\frac{\partial C_X}{\partial M_1}\mathcal{P}_{M_1}\right)^2 + \left(\frac{\partial C_X}{\partial S}\mathcal{P}_S\right)^2\right]^{\frac{1}{2}}\end{aligned}$$

In these expressions, the $\mathcal{P}$ symbols represent the precision error of the respective variables represented by the subscripts. These errors are derived from the measured data.

The overall uncertainty for each of the coefficients is obtained by calculating the root sum square of the bias and precision errors for each coefficient. Thus, for example, the uncertainty in the axial force coefficient is given by:

$$\mathcal{U}_{C_X} = \left[(\mathcal{B}_{C_X})^2 + (\mathcal{P}_{C_X})^2\right]^{\frac{1}{2}} \qquad (12)$$

Pressure Uncertainty

The approach to calculating the uncertainty in the pressure data parallels the approach used for the force and moment coefficients. Again, the bias and precision errors must be accounted for. As noted earlier, the pressure data are normalized with respect to the free-stream static pressure P_1. Thus:

$$\begin{aligned}r &\equiv \frac{P}{P_1} = \frac{P}{P_{t1}}\frac{P_{t1}}{P_1} = \frac{P}{Pt1}\left(1 + \frac{\gamma - 1}{2}M_1^2\right)^{\frac{\gamma}{\gamma-1}} \quad (13)\\ &= \left(\frac{P_g + P_{atm}}{P_{t1}}\right)\left(1 + \frac{\gamma - 1}{2}M_1^2\right)^{\frac{\gamma}{\gamma-1}}\end{aligned}$$

We note that the normalized static pressure, r, is a function of the static gauge pressure P_g measured by the transducer, the stagnation pressure P_{t1}, the atmospheric pressure P_{atm}, and the free-stream Mach number M_1.

Therefore, expressions for the bias and precision errors for the normalized static pressure are:

$$\begin{aligned}\mathcal{B}_r &= \left[\left(\frac{\partial r}{\partial P_g}\mathcal{B}_{P_g}\right)^2 + \left(\frac{\partial r}{\partial P_{atm}}\mathcal{B}_{P_{atm}}\right)^2\right. \qquad (14)\\ &\quad \left. + \left(\frac{\partial r}{\partial P_{t1}}\mathcal{B}_{P_{t1}}\right)^2 + \left(\frac{\partial r}{\partial M_1}\mathcal{B}_{M_1}\right)^2\right]^{\frac{1}{2}}\end{aligned}$$

$$\begin{aligned}\mathcal{P}_r &= \left[\left(\frac{\partial r}{\partial P_g}\mathcal{P}_{P_g}\right)^2 + \left(\frac{\partial r}{\partial P_{atm}}\mathcal{P}_{P_{atm}}\right)^2\right. \qquad (15)\\ &\quad \left. + \left(\frac{\partial r}{\partial P_{t1}}\mathcal{P}_{P_{t1}}\right)^2 + \left(\frac{\partial r}{\partial M_1}\mathcal{P}_{M_1}\right)^2\right]^{\frac{1}{2}}\end{aligned}$$

Finally, the uncertainty in the normalized static pressure is given by:

$$\mathcal{U}_r = \left[\mathcal{B}_r^2 + \mathcal{P}_r^2\right]^{\frac{1}{2}} \qquad (16)$$

Example:

To illustrate application of the procedure for obtaining the uncertainty, we apply it to a data set obtained from the AFB/APB models during the experimental program. The nominal test conditions are:

α	6°
P_{t1}	176.12 psia
M_1	4.28
P_{atm}	11.333 psia
S	$0.8882 in^2$
X	$0.952 lb_f$
P_{g_4}	$-10.706 lb_f/in^2$

We will calculate the uncertainty $\mathcal{U}_X$ and the percent uncertainty $\%\mathcal{U}_X$ of the axial force coefficient.

We will also calculate the values of the same variables for the normalized static pressure at pressure tap #4. Analogous calculations can be accomplished for the normal and pitching moment coefficients.

Proceeding, we take the appropriate derivatives of eq. 7, substitute nominal values for the variables, and arrive at the following results:

$$\begin{aligned} \frac{\partial C_X}{\partial X} &= 0.109/lb_f \\ \frac{\partial C_X}{\partial M_1} &= 8.497 \times 10^{-3} \\ \frac{\partial C_X}{\partial P_{t1}} &= -5.904 \times 10^{-4} in^2/lb_f \\ \frac{\partial C_X}{\partial S} &= -0.117/in^2 \end{aligned}$$

The bias values for each independent variable are taken from instrumentation and facility calibration data and are:

$$\begin{aligned} \mathcal{B}_X &= 0.033 lb_f \\ \mathcal{B}_{M_1} &= 0 \\ \mathcal{B}_{P_{t1}} &= 0.05 lb_f/in^2 \\ \mathcal{B}_S &= 8.88 \times 10^{-4} in^2 \end{aligned}$$

Substituting the above values into eq. 10 yields:

$$\mathcal{B}_{C_X} = 3.66 \times 10^{-3} \qquad (17)$$

The precision errors are obtained from the standard deviation values of each variable. The standard deviation values are obtained from the raw data. For this example:

$$\mathcal{P}_X = 2\mathcal{S}_X = 2(8.58 \times 10^{-4}) = 1.72 \times 10^{-3} lb_f$$

$$\mathcal{P}_{P_{t1}} = 2\mathcal{S}_{P_{t1}} = 2(0.253) = 0.51 lb_f/in^2$$

$$\mathcal{P}_{M_1} = 0.04$$

$$\mathcal{P}_S = 0$$

The $\mathcal{P}_{M_1}$ value is based on a facility calibration program accomplished prior to this experimental program. The uncertainty in S has been accounted for in the bias error and the precision error has been zeroed here. Substituting into eq. 11 yields:

$$\mathcal{P}_{C_X} = 4.88 \times 10^{-4}$$

The uncertainty is thus:

$$\mathcal{U}_{C_X} = \left[(\mathcal{B}_{C_X})^2 + (\mathcal{P}_{C_X})^2\right]^{\frac{1}{2}} = 3.69 \times 10^{-3}$$

Nominally:

$$C_X = 0.1061$$

Hence:

$$\%\mathcal{U}_{C_X} = \frac{3.69 \times 10^{-3}}{1.061 \times 10^{-1}} \times 100 = 3.48$$

Thus, for this example, we can state:

$$C_X = 0.1061 \pm 0.00037$$

Continuing with the example, we calculate the uncertainty in the normalized static pressure. Calculating the appropriate derivatives of r in eq. 14 using eq. 13 and the nominal values for this example, we get:

$$\begin{aligned} \frac{\partial r}{\partial P_g} &= 1.244 in^2/lb_f \\ \frac{\partial r}{\partial P_{t1}} &= -4.43 \times 10^{-3} in^2/lb_f \\ \frac{\partial r}{\partial P_{atm}} &= 1.244 in^2/lb_f \\ \frac{\partial r}{\partial M_1} &= 1.00 \end{aligned}$$

The bias values are:

$$\begin{aligned} \mathcal{B}_{P_g} &= 0.024 lb_f/in^2 \\ \mathcal{B}_{P_{t1}} &= 0.05 lb_f/in^2 \\ \mathcal{B}_{P_{atm}} &= 0.007 psia \\ \mathcal{B}_{M_1} &= 0 \end{aligned}$$

Substituting into eq. 14 yields:

$$\mathcal{B}_r = 0.0311$$

The precision errors for the independent variables associated with the normalized static pressure obtained from the raw data are:

$$\mathcal{P}_{P_g} = 2\mathcal{S}_{P_g} = 2(6.02 \times 10^{-3}) = 1.204 \times 10^{-2} lb_f/in^2$$

$$\mathcal{P}_{P_{t1}} = 2\mathcal{S}_{P_{t1}} = 2(0.210) = 0.42 lb_f/in^2$$

$$\mathcal{P}_{P_{atm}} = 0$$

$$\mathcal{P}_{M_1} = 0.04$$

Substituting into eq. 15 gives:

$$\mathcal{P}_r = 0.043$$

The uncertainty is thus:

$$\mathcal{U}_r = \left[\mathcal{B}_r^2 + \mathcal{P}_r^2\right]^{\frac{1}{2}} = 0.053$$

Nominally:

$$r_4 = 0.783$$

Hence:

$$\%\mathcal{U}_r = \frac{0.053}{0.783} \times 100 = 6.77$$

Thus, for this example, we can state:

$$r = 0.783 \pm 0.053$$

We can summarize the results for this example as follows:

$$\begin{aligned}
\mathcal{B}_{C_X} &= 3.66 \times 10^{-3} \\
\mathcal{B}_r &= 3.14 \times 10^{-2} \\
\mathcal{P}_{C_X} &= 4.88 \times 10^{-4} \\
\mathcal{P}_r &= 0.043 \\
\mathcal{U}_{C_X} &= 3.69 \times 10^{-3} \\
\mathcal{U}_r &= 0.053 \\
C_X &= 0.1061 \pm 0.00037 \\
r_4 &= 0.783 \pm 0.053 \\
\%\mathcal{U}_{C_X} &= 3.48 \\
\%\mathcal{U}_r &= 6.77
\end{aligned}$$

Results of calculations like the ones in this example are used to generate the error bars in the plots in this report.

CFD - The Cobalt$_{60}$ code

Flow fields for the PLES configurations in a Mach 4.28 air-stream were computed using the December 1999 version of the Cobalt$_{60}$ code that had been developed by the Computational Sciences Branch at the U.S. Air Force Research Laboratory.[13] The aerodynamic parameters, thus computed, were compared with the corresponding experimentally-determined aerodynamic parameters. Cobalt$_{60}$ is an implicit, parallel code that can be used to solve the full Navier Stokes equations, or simplifications thereof. The code can be set up to neglect the presence of a boundary layer adjacent to the surface, i.e., it can be set up to solve the Euler equations. In addition, the code can be set up, assuming that the boundary layer remains laminar over the entire surface of the configuration or that it transitions to turbulent flow at pre-defined locations on the surface. If transition is assumed to occur, the user of the code can select from a variety of turbulence models. The turbulence models available at the time these computations were made were: the one-equation turbulence model of Spalart and Allmaras[15] and the one-equation model of Baldwin and Barth.[16] Flow fields were computed for the three possible boundary-layer models: no boundary layer (using the Euler equations), a fully-laminar boundary layer, and a fully-turbulent boundary layer, so that no portion of the boundary layer is laminar. The Spalart-Allmaras turbulence model was used for those cases, where the boundary layer was assumed to be turbulent.

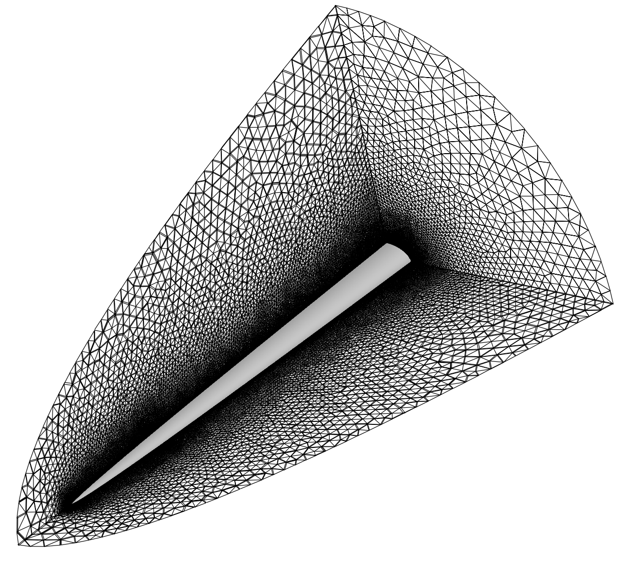

Fig. 7 Cobalt$_{60}$ unstructured grid generated by VGRIDns for 0° angle of attack.

The unstructured grids that were used for the present study were generated using Gridgen, GRIDTOOL, and VGRIDns.[17] In order to minimize the computational resources required, the grid generation strategy took advantage of flow-field symmetry, where possible. One can take advantage of the fact that the zero angle-of-attack flow field is symmetric about both the pitch plane and the yaw plane. Thus, as shown in Fig. 7, one needs to generate an unstructured grid for only one quadrant of the flow field. For the present study, approximately one-million cells were used to compute the flow field, when the configuration is at zero angle-of-attack. For those cases where the angle-of-attack is not zero, but the yaw angle is, the grid-generation scheme took advantage of the fact that the flow was planar symmetric about the pitch plane. Thus, the grid was mirrored about the yaw plane to provide a half-model of the flow field that contained approximately two-million cells.

The inflow boundary conditions were taken to be those for the nominal test conditions for the runs that were conducted in the TWT. Flow-field solutions were computed for "all" angles-of-attack and for "all" configurations at $P_{t1} = 175 psia$. Flow-field solutions were computed for selected configurations at $P_{t1} = 150 psia$ and at $P_{t1} = 240 psia$. These computations were made to investigate, if there were any Reynolds-number effects evident in the computed solutions.

The far-field boundaries were located far enough

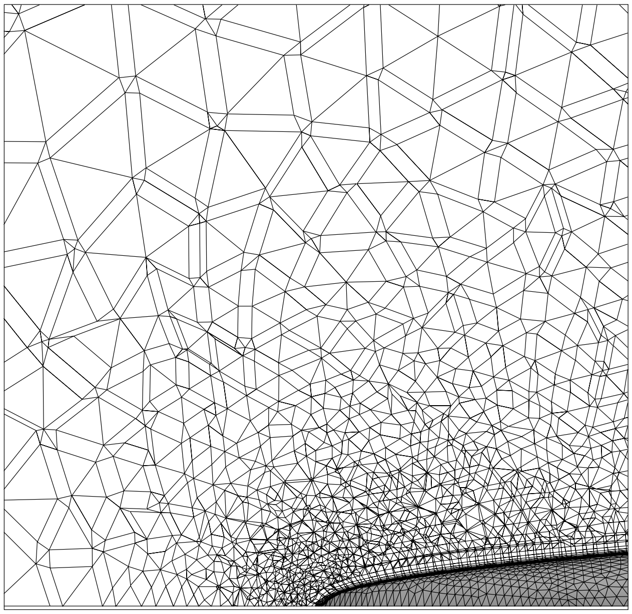

Fig. 8 Detail of Cobalt$_{60}$ grid near the nose.

from the surface of the model so that the entire bow-shock wave could be captured over the entire angle-of-attack range, of interest to the present study. I.e., the entire shock layer could be computed for angles-of-attack from $-11°$ to $+11°$. A close up of the unstructured grid in the vicinity of the model apex is presented in Fig. 8. The area covered in Fig. 8 corresponds to x in the range of ± 0.5 inches. As can be seen in Fig. 7, the downstream boundary of the grid is co-planar with the base of the PLES configuration. Thus, the effect of base flow is not modeled in these calculations. When calculating the axial force acting on the model, it was assumed that pressure that acts over the base area of the model is equal to the free-stream static pressure.

Results and Discussion

The comparison between the experimentally-determined aerodynamic parameters and the corresponding computed values are presented in this paper in four sections. Surface-pressure measurements that were obtained at an angle-of-attack of 0°, ±6°, and ±10°/ ± 11° and flow-visualization photographs will be presented in the first three sections. The values of the experimentally-determined parameters and of the computed parameters will be used to define the three different flow fields that occur over the range of alpha considered in the present paper. When the angle-of-attack is zero, the flow field should be symmetric about both the xy-plane and the xz-plane. Six degrees angle-of-attack corresponds approximately to the upper limit for which the normal force coefficient is a linear function of the angle-of-attack. The third section will focus on the flow fields for the relatively high angles-of-attack, i.e., ±10°/ ± 11°, where the flow field contains multiple vortices that result from flow separation. The force- and the moment-data will be discussed in the fourth and final section.

Φ	Shock Dist. from CL ($x = 4.5$)		Shock Dist. from CL ($x = 9.0$)		Shock angle	
	Expt.	CFD	Expt.	CFD	Expt.	CFD
0	1.55	2.8	1.557252	2.919848	15.5	15.1
30	1.50	2.7	1.563679	2.826651	15.9	15.5
60	1.55	2.8	1.621711	2.796053	16.0	15.0
90	1.55	2.85	1.619877	2.926229	16.0	15.6
120	1.55	2.65	1.667308	2.746154	15.9	14.9
150	1.55	2.70	1.586423	2.780076	16.0	14.8
180	1.50	2.70	1.605916	2.919848	16.0	16.2
270	1.60	2.80	1.623822	2.886795	15.8	16.1

Table 5 H3 shock angle comparison

The Flow Field for 0° Angle-of-Attack

Surface streamlines that were observed in the oil-flow patterns obtained with the model at zero angle-of-attack and which are not presented in this paper, were essentially parallel to the (vertical) pitch plane-of-symmetry. Thus, the oil-flow patterns indicated that there was some cross flow. As was noted in the Introduction, Kontis et al.[1] reported "the presence of a cross-flow from the high pressure sides at the ends of the major axis to the low pressure sides at the ends of the minor axis".

Cross flow also affected the shape of the bow shock wave. Mach-number contours that were computed using the Cobalt$_{60}$ code for a $Re_L = 14.55 \times 10^6$, which corresponds to a stagnation chamber pressure of 175 psia, are presented in Fig. 9 for the baseline configuration at cross sections of $x = 4.50$ inches and of $x = 9.00$ inches. The computed iso-Mach contours are approximately circular in cross section. The clustering of the iso-Mach contours corresponds to the location of the bow shock wave in the computed flow field. Schlieren photographs were obtained by Urena and Massett[18] while a power-law elliptic-section (PLES) model was rotated about its longitudinal, x-axis. Urena and Massett[18] also used a PLES model for which $z(x)$ and $y(x)$ vary as the one-half power-law, as given in equations 1 and 2, respectively. Since the model used in Ref.[18] had a thickness ratio that was 1.60 times the thickness ratio of the baseline configuration, $C_1 = 0.190$ and $C_2 = 0.317$. Schlieren photographs were taken while varying the roll angle in thirty-degree increments. The trace of the bow shock wave in each schlieren photograph was used to generate an experimental definition of the bow-shock-wave contours in the plane of $x = 4.50$ inches and in the plane of $x = 9.00$ inches. The experimentally-determined cross sections thus determined for the bow shock wave are compared with the computed cross sections in Fig. 10. The experimentally-determined cross sections are in good agreement with the computed iso-Mach contours. Using schlieren photographs, Kontis et al.[1] observed: "The distance between the shock wave and the body, for 0° incidence, is greater in the meridian plane con-

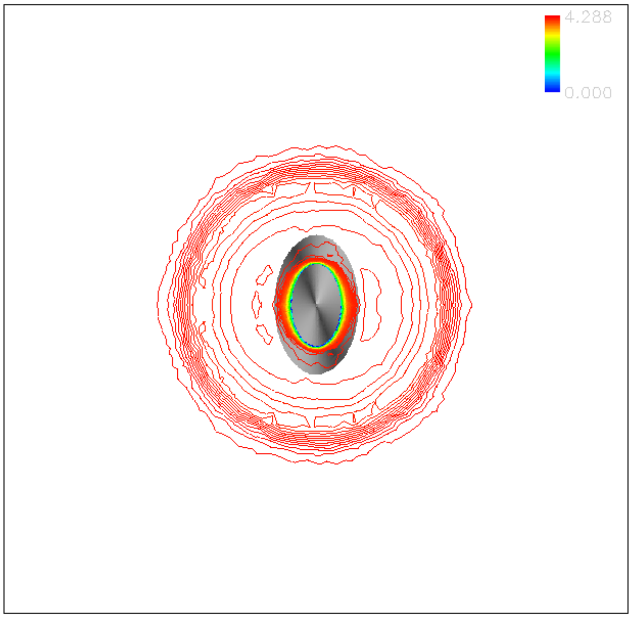

a) at $x = 4.5in$

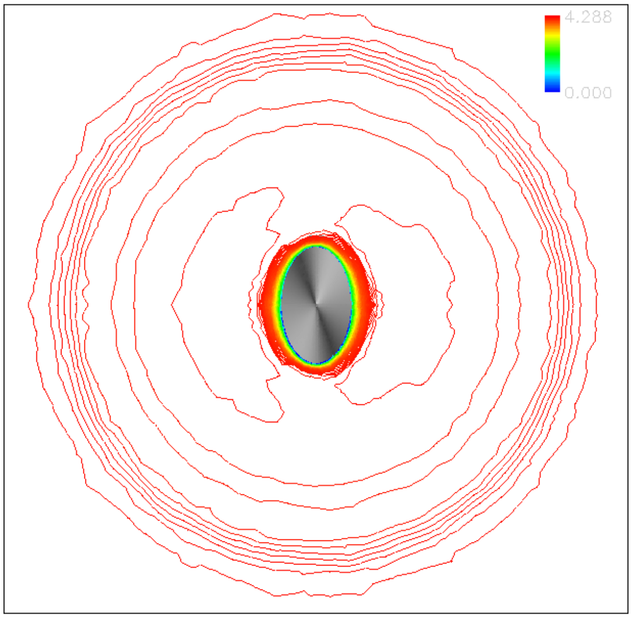

b) at $x = 9.0in$

Fig. 9 Cobalt$_{60}$ calculated Mach coutours

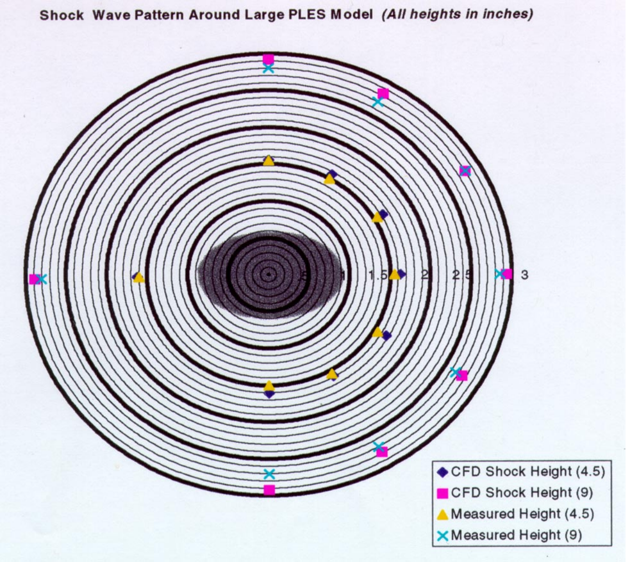

Fig. 10 Comparison of exerimental and computational shock shape measurements

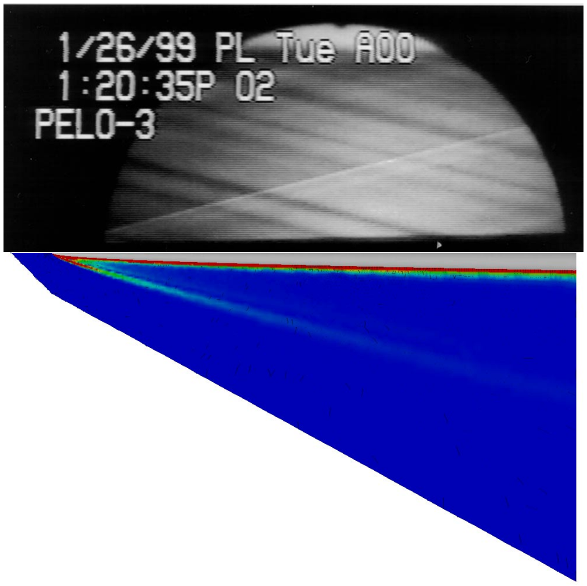

Fig. 11 The Bow Shock Wave at $\alpha = 0°$

taining the minor axis than in the meridian plane containing the major axis. The shock wave is not an ellipse similar to the body, but is 'pushed in' toward the major axis and is 'pulled out' from the minor axis." Thus, the results from the present investigation are consistent with the results reported by Kontis et al.[1]

The trace of the bow shock wave in the vertical pitch plane ($y = 0$) is presented in Fig. 11 for the baseline model at zero-angle-of-attack in a Mach 4.28 air-stream with $Re_L = 14.55 \times 10^6$. The schlieren photograph is the top portion of the figure. The computed flow is below the plane-of-symmetry. The experimentally-observed bow shock wave, as determined from the schlieren photograph, is in good agree-

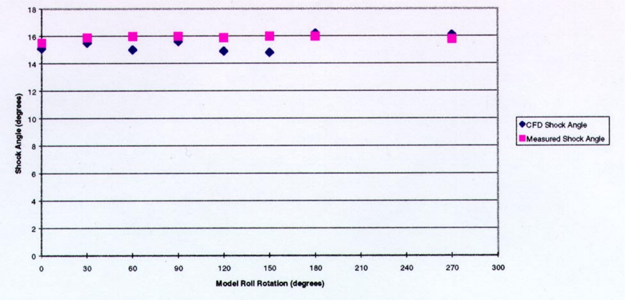

Fig. 12 Bow shock wave angle measurements

ment with that from the Cobalt$_{60}$ -computed flowfield solution. Note that the bow-shock-wave angle is curved near the apex of the model, but becomes a straight line (i.e., is linear) at points well downstream from the nose. Using the schlieren photographs that were obtained as the large-thickness-ratio model was rotated in thirty-degree increments, Urena and Massett[18] measured the bow-shock-wave angle in the linear region. The experimentally-determined values for the bow-shock-wave angle, thus determined, and the corresponding computed values are presented as a function of the roll angle ϕ in Fig. 12. The computed values and the experimentally-determined values are in reasonable agreement.

Thus, it is seen that, for zero angle-of-attack, the cross section of the bow shock wave is almost circular both for station $x = 4.50$ inches and for station $x = 9.00$ inches for the baseline model (see Figs. 9(a) and 9(b)) and for the relatively large thickness-ratio model (see Fig. 10). Furthermore, the slope of the bow shock wave in the linear region is almost independent of ϕ (see Fig. 12). Thus, one would expect the static pressures on the surface of the model to be "approximately constant" at each of the two cross sections for which data were obtained.

Pressure measurements obtained at zero angle-of-attack and with the total pressure equal to 175 psia are presented in Fig. 13(a) for four different runs, two with the Eglin-built model (EPB) and two with the Academy-built model (APB). The typical test procedure was to obtain zero-angle-of-attack pressures twice during each run, once during the sweep through negative angles-of-attack and once during the sweep through positive angles-of-attack. The surface-pressure measurements from the upstream station, i.e., the station at $x = 4.50$ inches, are represented by the filled symbols. The surface-pressure measurements from the downstream station, i.e., the station at $x = 9.00$ inches, are represented by the open symbols. As can be seen in the data of Fig. 13(a), the experimental value for any test condition is ±3% of the arithmetic average of the four measurements for that orifice. Thus, the run-to-run variations, i.e., the repeatability of the measurements are well within the potential variations due to experimental uncertainty.

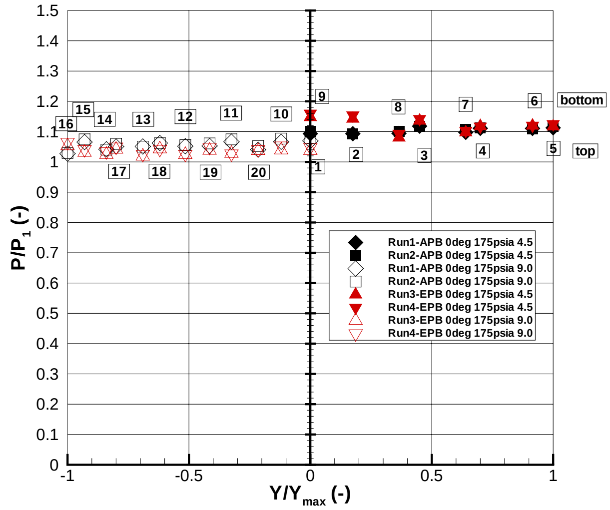

a) for the APB model and for the EPB model, with pressure taps labeled.

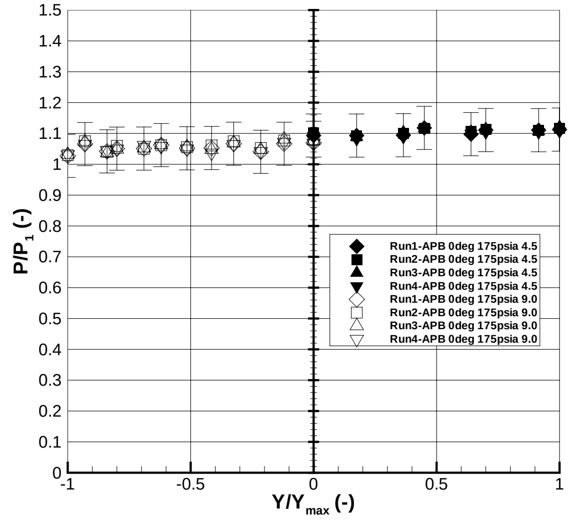

b) only for the APB model

Fig. 13 Pressure measurements illustrating the repeatability of the data for $\alpha = 0°$ and $P_{t1} = 175psia$

It should be noted that there appears to be no significant, consistent bias for the measurements that come from the orifices located on the top surface of the model (i.e., negative values of z) relative to the measurements from the orifices from the lower surface of the model (i. e., positive values of z). The static pressures measured at orifices 17 and 18 (on the top of the model) are slightly greater than the measurements for orifices 13 and 14 (on the bottom of the model). Referring to Table 3 and to Fig. 5 for the orifice locations, the reader can see these orifices are located at similar y/y_{max}. Conversely, the static pressures measured at orifice 20 (on the top of the model) are slightly less than the measurements for orifice 10 (on the bottom of the model).

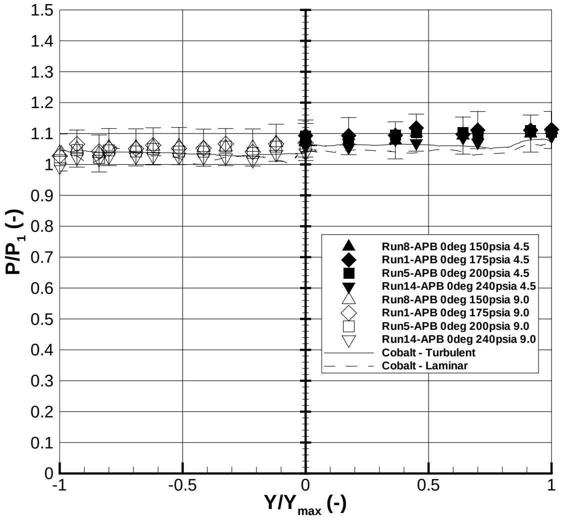

Fig. 14 The effect of Reynolds number on the spanwise pressure distribution for $\alpha = 0°$

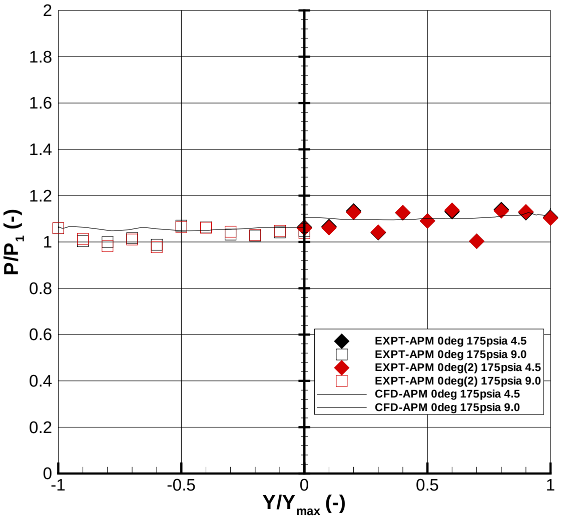

Fig. 15 Comparison of Pressures at 0° for the APM model with CFD

The spanwise pressure distributions from four different runs are presented in Fig. 13(b). However, unlike Fig. 13(a), all four data sets are for the same model, i.e., the APB. The run-to-run variations in the pressure measurements obtained at zero angle-of-attack and with the total pressure equal to 175 psia exhibit even smaller run-to-run variations than the measurements that were presented in Fig. 13(a).

Table 6 Slope of the baseline-model surface in the pitch plane (dz/dx) and in the yaw plane (dy/dx)

x-station	dz/dx	dy/dx
(in.)	(°)	(°)
4.50	1.607	2.674
9.00	1.136	1.891

For all of the data presented in Fig. 13, the pressure measurements from the station x = 4.50-inches, i.e., the filled symbols, are slightly greater than those from the station x = 9.00-inches, i.e., the open symbols. The slope of the baseline-model surface at these two x-stations is presented in Table 6, using eqn. 1 for the pitch plane, and using eqn. 2 for the yaw-plane. The slope of the model surface decreases with x. Thus, if one uses a simple impact theory to estimate the local static pressure, one would expect that the pressure would decrease with x. However, as has been discussed, the cross flow that occurs even at zero angle-of-attack modifies the structure of the shock wave and, therefore, the static pressures acting on the model surface. Again, subtle complexities exist in the flow field for this relatively simple shape at zero angle-of-attack.

Pressure measurements obtained with the APB model at zero angle-of-attack are presented for all four Reynolds numbers in Fig. 14. The pressure measurements are independent of the Reynolds number. Referring to Table 1, the reader will recall that, for the present tests, the Reynolds numbers based on the free-stream conditions and on the model length, ranged from 11.74×10^6 to 18.79×10^6. Although the authors do not have specific information about the boundary-layer transition criteria for this configuration, it is believed that the boundary layer would be turbulent over most of the model at each test condition. Thus, it is not surprising that the surface-pressure measurements do not depend on the Reynolds number for the range of conditions tested.

Included in Fig. 14 are the spanwise pressure distributions computed using the Cobalt$_{60}$ code for a total pressure of 175 psia. Flow field solutions were computed for three different models for the viscous boundary layer: (a) ignore the boundary layer altogether, i.e., solve the Euler equations (b) assume that the boundary layer remains laminar over the entire length of the model (c) assume that the boundary layer is fully turbulent along the entire length of the model There are no significant differences in the surface-pressure distributions computed for the three different models for the viscous boundary layer. Furthermore, the agreement between the computations and the measurements is considered to be very good.

The spanwise distributions of the static pressures for the APM configuration at zero angle-of-attack when the Reynolds number based on the free-stream condition and the model length is nominally 13.69×10^6 are presented in Fig. 15. The experimentally-determined values are in good agreement with the computed values. Recall that the thickness ratio of the APM model was 1.6 times the thickness ratio for the APB model. Thus, the thickness ratio does not appear to have a significant effect on the flow field, at least over the limited range of variation for the thickness ratio that was considered here.

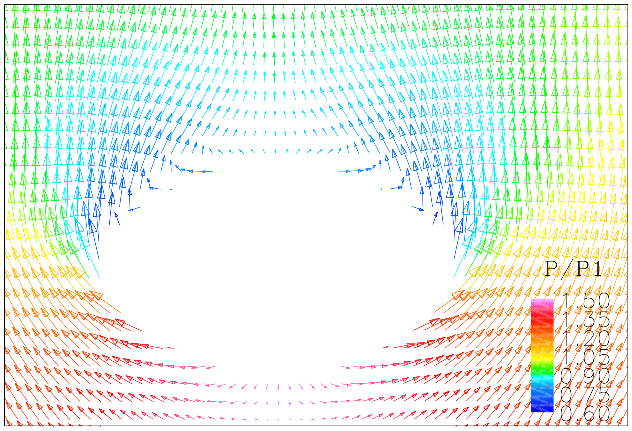

a) $x = 4.50in.$

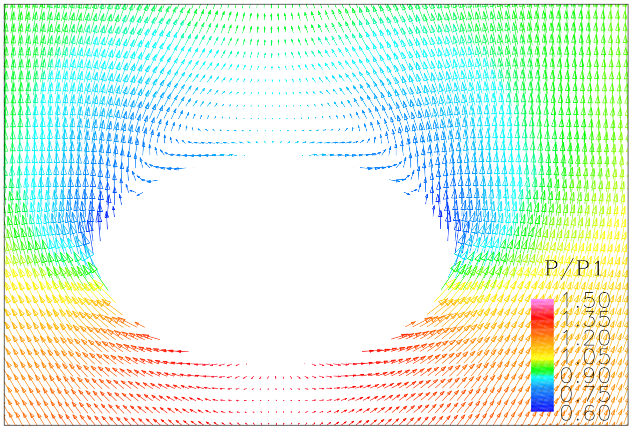

b) $x = 9.00in.$

Fig. 16 Vector components of the velocity in planes of constant x (cross-section planes)

The Flow Field for 6° Angle-of-Attack

Referring to Fig. 16, the reader can see that cross-flow separation occurs at an angle-of-attack of 6°. The vector components of the velocity, as computed for planes of constant x, i.e. $x = 4.5$ inches and $x = 9.0$ inches, clearly indicate that the flow separates from the upper surface of the elliptic cross section in the vicinity of $y/y_{max} = 0.8$. Later in this section, we will see that an angle-of-attack of six degrees is slightly above the alpha range for which the normal force coefficient is a linear function of the angle-of-attack.

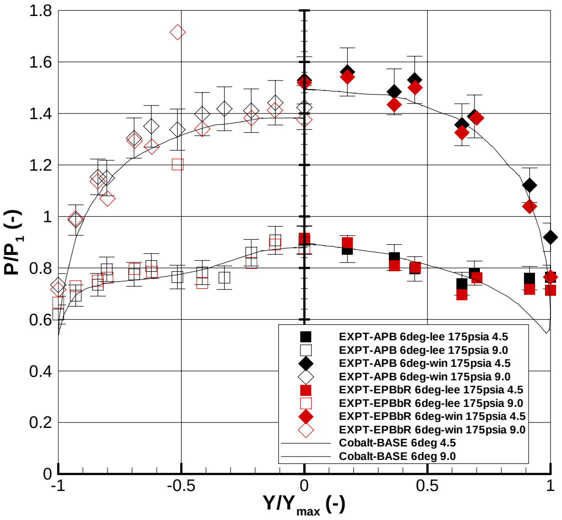

Fig. 17 Surface pressures for the APB abd EPB models at $\alpha = 6°$

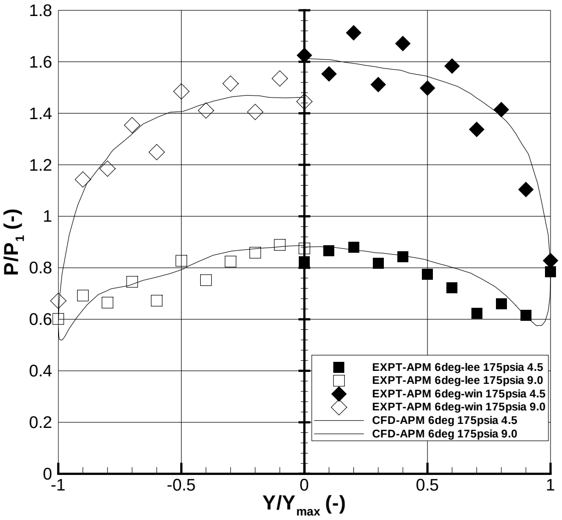

Fig. 18 Surface pressures for the APM model at $\alpha = 6°$

Experimentally-determined spanwise pressure distributions for the APB and for the EPB model are compared in Fig. 17 with the computations. These results are presented for a Reynolds number based on the free-stream conditions and the model length that is nominally 13.69×10^6. The measurements from the station $x = 4.50$ inches exhibit some scatter. In actuality, the three measurements from the region $0.15y_{max} \leq y \geq 0.70y_{max}$ that are greater than the computed values all were sensed at orifices located on the top of the models, i.e., having negative values of z. Conversely, the two pressure measurements from the region $0.15y_{max} \leq y \geq 0.70y_{max}$ that are very close in magnitude to the computed values are from the bottom of the models, i.e., having positive values of z. Since this is true both for the Academy-built model (APB) and for the Eglin-built model (EPB), the difference is attributed to a flow field phenomena rather than a model-construction difference. Furthermore, measurements of the model offset, i.e., the actual angle-of-attack of the model before or after a run (when it should be zero), were taken on a regular basis. The model offsets were small, usually less than 0.2°, which was close to the uncertainty in our measurement. The differences between the pressures sensed at orifices on the top of the model and those from the bottom of the model far exceed what one would expect due to an error in the offset angle. Thus, the differ-

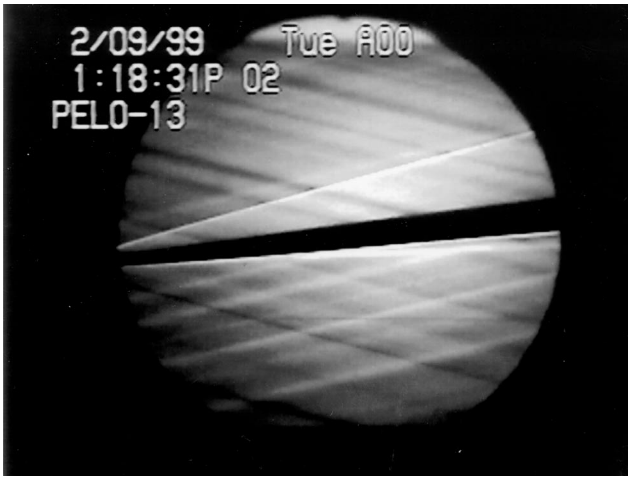

a) $\alpha = +6°$.

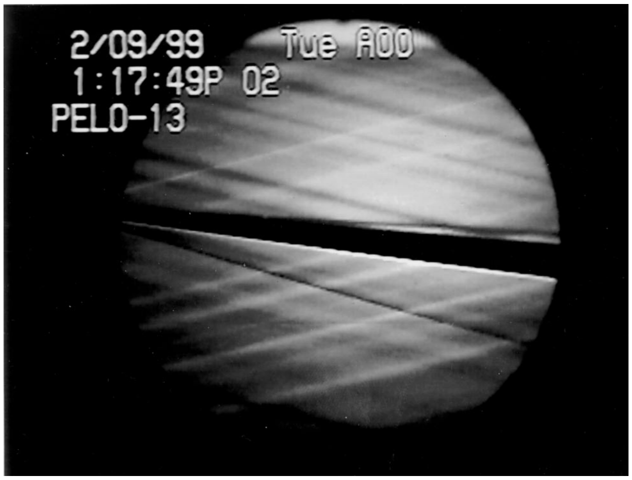

b) $\alpha = -6°$.

Fig. 19 Schlieren photographs for the flowfield for the baseline configuration at an angle of attack of $\pm 6°, P_{t1} = 175$**psia.**

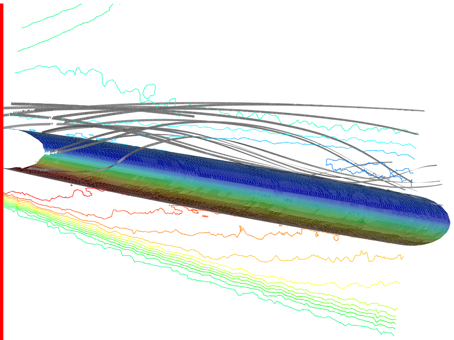

ences are attributed to weak waves crossing the tunnel, which could be seen in the schlieren photographs. The waves, which can be seen in Figs. 19, are attributed to small disturbances associated with the curvature of the nozzle wall, when the nozzle blocks were machined.

A horizontal line can be seen in the schlieren photographs originating near the middle of the leeside of the model. The horizontal trace can be seen both for the positive angle-of-attack (Fig. 19(a)) and for the negative angle-of-attack (Fig. 19(b)). It is believed that this trace marks the boundary of the coalescence of the recirculating viscous cross flow in the leeward plane-of-symmetry. There is no indication of significant density gradients in the schlieren photograph in the leeward flow upstream of the origin of this horizontal line. Thus, it is believed that, in the leeward flow near the nose, significant density gradients occur only in a thin, turbulent boundary layer.

a) Yaw-plane (side) view.

b) Leeward view.

Fig. 21 Oilflow at $\alpha = 10°$.

flow field than was evident in the computed solution. Presented in Fig. 21 are a side view and a leeward view of the oil-flow patterns obtained with the EFB model at an alpha of 10°. Note that the oil-flow patterns indicate the existence both of a primary- and of a secondary-separation location. The oil-flow pattern that appears in the side view of Fig. 21(a) indicates that a flow separation occurred very near the yaw plane as the flow proceeded from the windward surface around the rapid change in cross-section slope for large values of y. This is the primary separation location. The primary separation locations for several values of x are designated by the red symbols in Fig. 22. Near the nose of the model, the oil-flow patterns indicate that the primary separation location is on the leeward surface. Further downstream, away from the nose of the model, the primary separation of the flow from the model surface takes place in the yaw plane, i.e., at the end of the major axis. Shereda et al.[8] presented similar findings for the primary separation locations from their tests.

The free-shear-layer separation created a pair of helical vortices as the air particles in the free-shear-layer moved both toward the leeward plane of symmetry and down the length of the model. The two helical vortices are features both of the computed flow (refer to Fig. 20) and of the experimentally-observed flow field. The two recirculating, helical vortices coalesced in the leeward plane-of-symmetry and then impinged on the surface. The trace marked "Feature of Interest" in the schlieren photograph of Fig. 23(a) marks the experimentally-observed outer limit of the coalescing vortices. The trace "Feature of Interest" in Fig. 23(b) marks the locally high densities in the leeward plane-of-symmetry taken from the "schlieren option" for the computed flow field. It is believed that this trace in the computed flow field that is presented in Fig. 23(b) also corresponds to the location of the outer limit of the vortex pair coalescing in the leeward plane-of-symmetry. Information to support this assumption is presented in Fig. 24. In Fig. 24 selected streamlines have been added to the computed density contours that were presented in Fig. 23(b). Note that the maximum value of the negative z-coordinate for the helical vortices corresponds to the location of the "Feature of Interest" in the leeward plane-of-aymmetry. Grids have been placed in Figs. 23(a) and 23(b) at the two x-stations where the static pressure ports are located. The experimentally-determined locations of this trace (as taken from the schlieren photograph) are in reasonable agreement with the computed locations (as determined from the density-gradient contours).

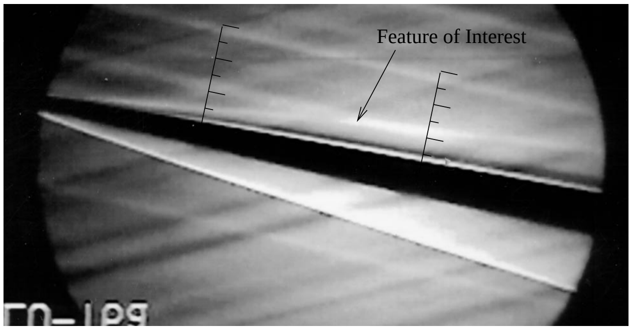

a) Experimental.

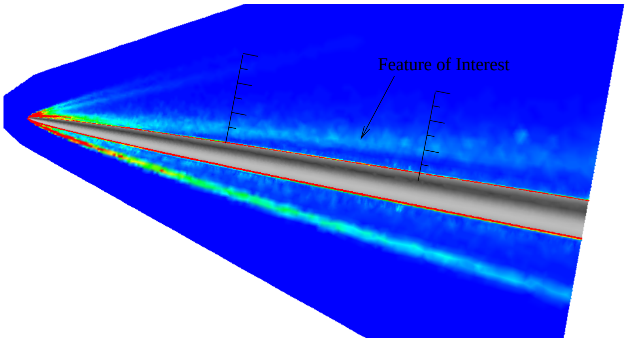

b) CFD (Cobalt$_{60}$ computations).

Fig. 23 Schlieren for $\alpha = 11°$.

As the two recirculating, helical vortices coalesced in the leeward plane-of-symmetry and then impinged on the surface, they created an attachment line in the leeward plane-of-symmetry. The reattaching flow

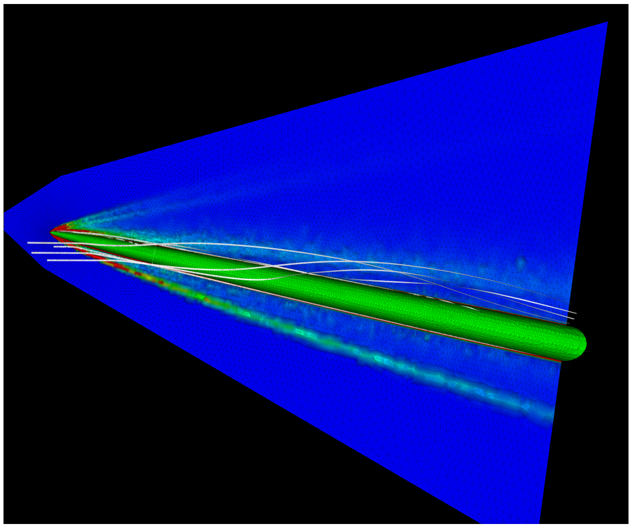

Fig. 24 Computed flowfield using schlieren option for $\alpha = 11°$ with streamlines added.

causes the pressures to be highest near the leeward plane-of-symmetry. See the spanwise pressure distribution presented in Fig. 25. On the leeward surface of the model, the recirculating flow proceeded both downstream and away from the plane-of-symmetry. As shown in Fig. 21(b), this flow produced a feather pattern in an oil film placed on the leeward surface. The oil-flow pattern is consistent with the pressure field. The spanwise component of the flow moved from the relatively high pressures near the leeward plane-of-symmetry. The pressure reached a minimum near the mid-span of the model, at $y \approx 0.5y_{max}$. As the spanwise component of the flow near the surface moved further from the plane of symmetry, it encountered an adverse pressure gradient. Refer to Fig. 25. The oil-flow patterns of Fig. 20b indicate that a second, imbedded free-vortex-type separation occurred long before the recirculating flow reached the yaw plane. As can be seen in Fig. 21(b), oil accumulated along a line approximately 2/3 of the way to the edge of the model in the yaw plane. Because the oil continued to flow downstream, it is believed to be the demarcation line of an imbedded free-vortex-type of separation for the recirculating flow, the secondary separation. Thus, even for a relatively low angle-of-attack, i. e., 10°, the flow field around the power-law elliptical-section configuration contains both primary and secondary separation streamlines. The locations of the secondary separation location are indicated by the blue symbol in Fig. 22. Oil-flow patterns presented by Shereda et al.[8] also exhibited secondary flow separation from the leeward surface.

The experimentally-determined spanwise pressure distributions for the APB and the EPB models at angles-of-attack of ±11° are presented in Fig. 25. Consider the experimentally-determined pressures for $x = 9.00$ inches, for which y is negative. The measurements from the top of Sta. 9.0 inches are on the leeward

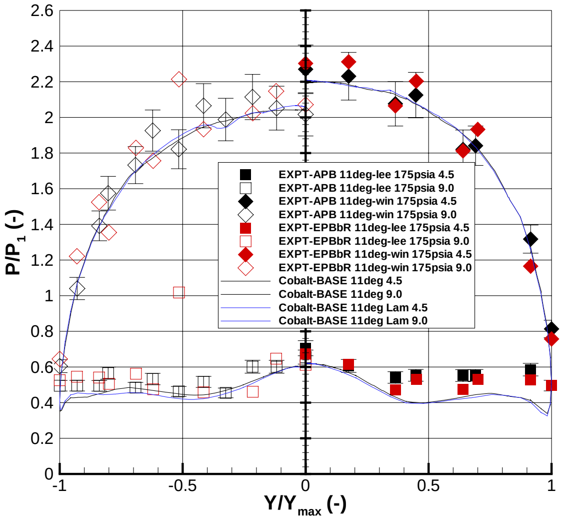

Fig. 25 Surface pressures for the APB abd EPB models at $\alpha = 11°$

surface, when the model is at an angle-of-attack of 11° (as represented by the filled diamonds). Similarly, the measurements from the bottom of Sta. 9.0 inches are on the leeward surface, when the model is at an angle-of-attack of −11° (as represented by the open squares). Note that, although these measurements are from two different stops on the alpha-sweep, a single smooth curve through the two sets of data would represent the experimentally-determined spanwise pressure distribution for the leeward surface. However, there are slight differences for the two sets of pressure measurements for the windward surface at Sta. 9.0 inches. Although the differences were well within the experimental uncertainty, the measured values for the bottom surface at Sta. 9.0 (as represented by the filled squares) were slightly greater than the measured values from the top surface of Sta. 9.0, when the model is at −11° angle-of-attack (as represented by the open diamonds). Refer to the schlieren photographs presented in Figs. 26(a) and 26(b). A weak right-running wave can be seen impinging on the windward surface of the model, when the model is at +11° angle-of-attack. The wave impinges on the model at Sta. 9.0, which corresponds to the location of the relatively high pressure measurements. The viscous/inviscid interaction associated with the weak impinging wave would explain the slight increase in these pressure measurements.

Force and Moment Data

The normal force coefficients for the baseline model built at the USAFA as measured at positive angles-of-attack are presented in Fig. 27 for all four Reynolds numbers. The measured values for the normal force coefficient are independent of the Reynolds number over the range for which data were obtained. Included for comparison are the normal force coefficients computed using the Cobalt$_{60}$ code. CFD solutions were ob-

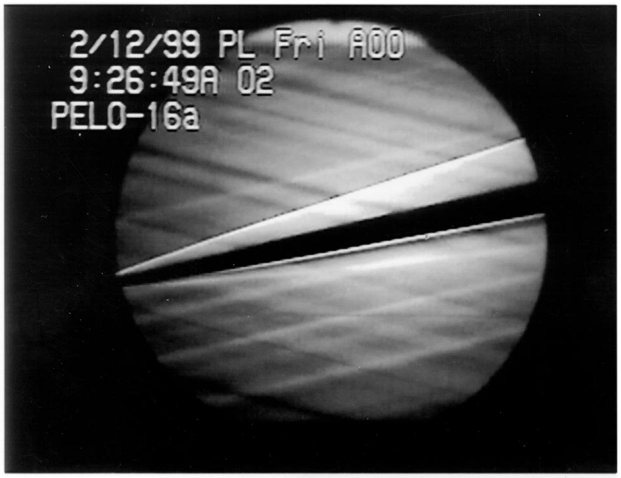

a) $\alpha = +11°$.

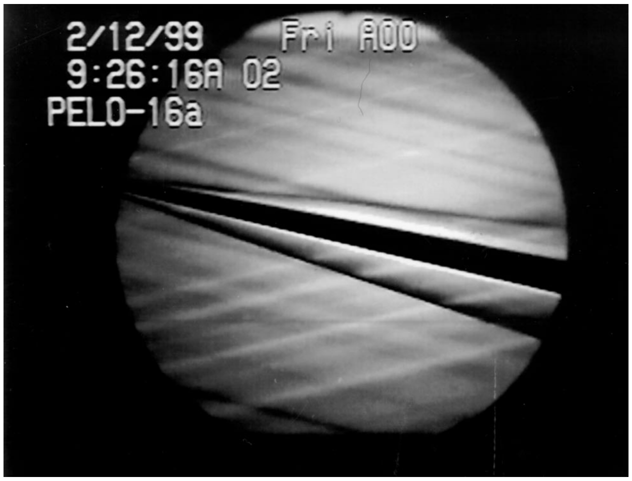

b) $\alpha = -11°$.

Fig. 26 Schlieren photographs for the flowfield for the baseline configuration at an angle of attack of $\pm 11°, P_{t1} = 175$psia.

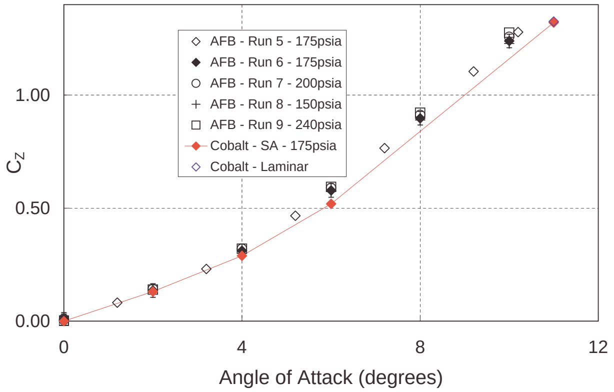

Fig. 27 Normal force for an H3 model

tained under the assumption that the boundary layer was fully laminar or that it was fully turbulent, using the turbulence model of Spalart and Allmaras.[15] For angles-of-attack of four degrees, or less, the lift coefficient is a linear function of the angle of attack, with the experimental values being slightly greater than computed values at a given angle-of-attack. For the angle-of-attack range where the normal force coefficient is a linear function of the angle-of-attack, the computational solutions indicate $C_{Z\alpha}$ is 0.0722 per degree whether the boundary layer is assumed to be fully laminar or fully turbulent. The corresponding value of $C_{Z\alpha}$ based on the experimental measurements is approximately 0.080 per degree. For the range of alpha, where the $C_{Z\alpha}$ is not constant, the differences between the experimentally-determined normal force coefficients and those computed assuming that the boundary layer is fully turbulent, although small, increase with alpha. Although the boundary layer is believed to be turbulent at the high Reynolds numbers associated with this study, the normal force coefficients computed assuming the boundary layer is wholly laminar are in relatively good agreement with the experimental values at 11°.

The experimentally-determined axial force coefficients, $C_{X,eff}$, for the baseline model built at the USAFA (AFB) are compared with the computed values in Fig. 28. The computed axial force component assumes that the pressure acting on the base of the model is equal to the free-stream static pressure. Therefore, in order to allow a direct comparison between the experimentally-determined axial force coefficients and the computed values, it is necessary to apply a correction to the to the experimental results.

The axial force, X, that is measured by the force balance, is the difference between the net force acting on the forward facing surfaces, X_{fore}, and the force acting on the base of the model. During the force-and-moment tests, two static pressure probes were located adjacent to the model-support sting in the base region of the model. Averaging the pressures sensed by these two probes yields an average value for the experimental base pressure, $P_{b,ave}$. The area over which the average value of the two base-pressure measurements acts is assumed to be the total base area of the model, S. Therefore, X is given by the following equation:

$$X = X_{fore} - P_{b,ave} S \tag{18}$$

Therefore, it is possible to calculate the force acting only on the forward facing surface of the model:

$$X_{fore} = X + P_{b,ave} S \tag{19}$$

Instead of using the average value of the two base-pressure measurements to calculate the force acting on the base of the model, let us assume that the free-static pressure acts on the base of the model. Assuming that

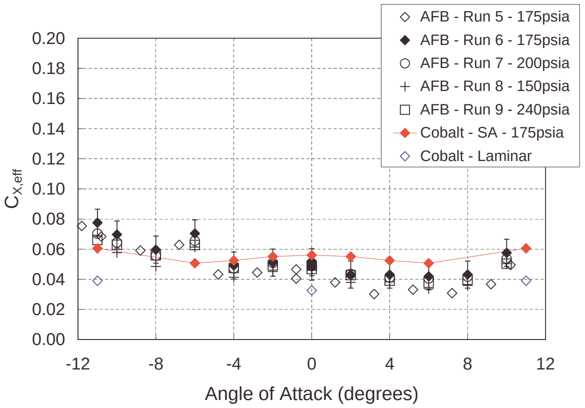

Fig. 28 Effective axial force for an H3 model

P_1 acts on the base of the model, the effective axial force, X_{eff}, is equal to the force that would act on the base due to the free-stream static pressure subtracted from the force acting on the forebody.

$$X_{eff} = X_{fore} - P_1 S \tag{20}$$

The effective axial force coefficient can then be calculated as follows:

$$C_{X,eff} = \frac{X_{eff}}{q_1 S} \tag{21}$$

The experimental values of the effective axial force coefficient as determined using equation 21, are presented in Fig. 28. Experimentally-determined values of $C_{X,eff}$ are presented for all four Reynolds numbers (i.e., all four values of the stilling chamber pressure). Measurements from two runs at a Reynolds number Re_L of approximately 13.69×10^6 (or $P_{t1} = 175$ psia) are in good agreement at the large negative angles-of-attack, but differ significantly as the angle-of-attack is increased. Recall that the stilling chamber pressure is held constant during a run. Furthermore, the force-and-moment measurements for a given angle-of-attack are recorded while the model pauses at the desired angle-of-attack during an alpha sweep. Note that the angle-of-attack for the measurements from Run 5 are offset 0.8° from all of the other data. Since the offset angle was measured before and/or after a run, this large offset indicates that the angle-of-attack changed significantly during this run. The angle-of-attack sequence for which the data of run 5 were obtained, started at a control input value of zero, swept to $-11°$, went to $+11°$, and then swept back to zero. Thus, the data from the alpha points early in the sequence (the negative angles-of-attack) are in relatively good agreement with the data from run 6. The differences between the run 5 measurements and the run 6 measurements are greater for the data from the alpha points late in the sequence (the positive angles-of-attack). Because of the time-dependent nature of the differences between the data from run 5 and those from run 6 and because of the relatively large offset angle, the authors believe that the model was not properly mounted for run 5 and the data from this run are considered anomalous.

The values of the effective axial force coefficient, as computed using the Cobalt$_{60}$ code, are included in Fig. 28. Computations are presented for two boundary-layer models: (1) the boundary layer is entirely laminar and (2) the boundary layer is entirely turbulent, using the Spalart and Allmaras turbulence model.[15] As would be expected for this slender body operating at relatively low angles-of-attack, the laminar values for $C_{x,eff}$ are significantly less than the turbulent values. The values of $C_{x,eff}$ that were computed assuming the boundary layer was wholly turbulent decrease slightly as the absolute value of the angle-of-attack goes from zero to six degrees, where it is a minimum. The effective axial force coefficient then increases with alpha. This angle-of-attack dependence for $C_{x,eff}$, first decreasing with alpha to a minimum, then increasing with alpha is believed to reflect the changing role of the skin-friction component of drag relative to the form drag component.

With the exception of the data obtained at an angle-of-attack of $-6°$, the experimentally-determined values of the effective axial force coefficient, $C_{X,eff}$, for negative angles-of-attack agree closely with the computations for the wholly turbulent boundary layer, both in magnitude and in their angle-of-attack dependence. For positive angles-of-attack, the alpha dependence of the experimentally-determined values of $C_{X,eff}$ is similar to that for the turbulent computations. However, the experimentally-determined values are less than the computed values assuming that the boundary layer is wholly turbulent. Thus, the experimental values of $C_{X,eff}$ exhibit an asymmetry between the data obtained at positive and negative angles-of-attack. For some of the runs, the two base pressure measurements were approximately equal, both in magnitude and in alpha dependence. For other runs, the two base pressure measurements were significantly different at certain angles-of-attack. Thus, the authors believe that a significant contributor to the difference between the experimentally-determined value of $C_{X,eff}$ at a given positive angles-of-attack and its value at the corresponding negative angle-of-attack is due to an anomaly in the base-pressure measurements.

The pitching moment coefficient about the apex is presented as a function of the positive angles-of-attack in Fig. 29 for all four Reynolds numbers. The measured values for the pitching moment coefficient are independent of the Reynolds number over the range for which data were obtained. Included for comparison are the pitching moment coefficients computed using

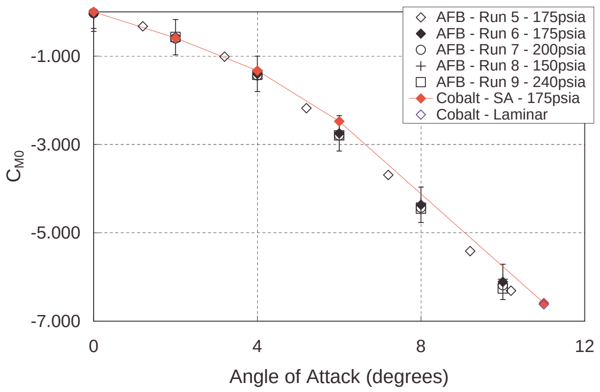

Fig. 29 Pitching moment coefficient around the apex for the AFB model as a function of alpha

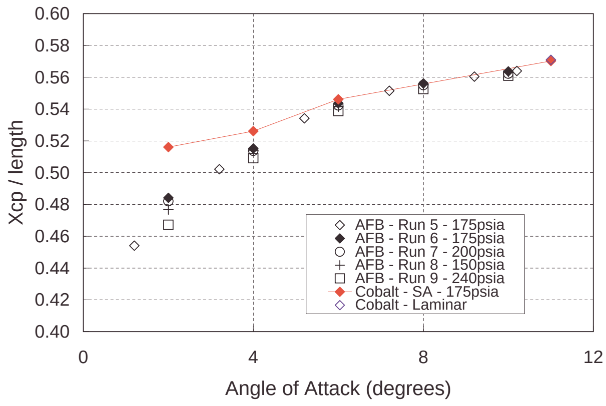

Fig. 30 The location of the center of pressure as a function of alpha

the Cobalt$_{60}$ code. CFD solutions were obtained under the assumption that the boundary layer was fully laminar or that it was fully turbulent, using the turbulence model of Spalart and Allmaras.[15] The differences between the experimentally-determined pitching moment coefficients and those computed assuming that the boundary layer is fully turbulent, although small, increase with alpha. Although the boundary layer is believed to be turbulent at the high Reynolds numbers associated with this study, the pitching moment coefficients computed assuming the boundary layer is wholly laminar are in relatively good agreement with the experimental values at 11°.

The movement of the center of pressure with angle-of-attack for the baseline model is presented in Fig. 30. The center of pressure is located at just over $x/L = 0.5$ and x_{cp}/L increases slightly as the magnitude of the angle-of-attack increases. This is in good agreement with the results of Edwards and Roper,[10] which indicated the center of pressure was at a position of $x/L = 0.56$.

Concluding Remarks

The following conclusions can be drawn regarding the flow field, based on the experimental data and on the flow-field computations discussed in the present paper over the range of conditions studied.

1. The zero-angle-of-attack pressure measurements from the top surface and from the bottom surface follow a single, well-behaved curve at each station, both in magnitude and in their dependence on y. Thus, the experimentally-determined pressure measurements indicate that both the model and the wind-tunnel flow field are symmetric about the xy-plane, i.e., the yaw plane.

2. For a given value of y/y_{max}, the pressure measured in the upstream plane, i.e., at $x = 4.50$ inches, is slightly greater than the pressure measured in the downstream plane, i.e., at $x = 9.00$ inches. This is true for both the measured pressures and for the computed pressures. This should be expected since the local surface inclination angle decreases with distance from the apex of the model.

3. The normal force coefficient is a linear function of the angle-of-attack for values of alpha in the range $\pm 4°$. The components of the velocity vectors taken from the Cobalt$_{60}$ -computed flow field for a plane of constant x indicate cross-flow separation, i.e., a free-vortex shear-layer separation, occurs at an angle-of-attack of 6°. Over the entire angle-of-attack range for which data were obtained, the normal force coefficients, the pitching moment coefficients, and the center of pressure locations were independent of the Reynolds number, or equivalently, the total pressure in the stilling chamber.

4. The effective axial force coefficients are significantly affected by the Reynolds number. Values of the effective axial force coefficient from the flow fields computed using the Cobalt$_{60}$ code were significantly greater, when the boundary layer is assumed to be fully turbulent as compared to the computations made assuming that the boundary layer remains laminar along its entire length.

5. Oil-flow patterns that were observed on the surface of the baseline model at an angle-of-attack of 10° indicate a more complex flow field than was evident in the computed solution. Oil-flow patterns indicate the existence both of a primary- and of a secondary-separation location. The primary-separation location occurred very near the yaw plane as the flow proceeded from the windward

surface around the rapid change in cross-section slope for large values of y. The components of the velocity vectors taken from the Cobalt$_{60}$ - computed flow field for a plane of constant x indicate a single cross-flow separation, that is produced by the free-vortex shear-layer separation.

Acknowledgements

Any study of this kind could not be accomplished without a dedicated and talented Technical Staff. The authors are most grateful to Larry Lamblin, the Director of Tri-Sonic Tunnel Operations, to Bobby Hatfield, the craftsman who built and instrumented the models that were done at the U. S. Air Force Academy, and to Tim Hayden and to SSgt Buddy Johns, who provided the software support to facilitate the ever-changing data-reduction needs for the experimental program. This investigation could not have been completed without the dedicated cooperation and willingness to modify continually the test plan that this technical staff provided.

References

[1] Kontis, K., Stollery, J. L., and Edwards, J. A., "Hypersonic Effectiveness of Slender Lifting Elliptic Cones With and Without Strakes," AIAA Paper 97–0521, Jan. 1997, Presented at the 35th Aerospace Sciences Meeting and Exhibit, Reno, NV.

[2] Bertin, J. J., *Hypersonic Aerothermodynamics*, AIAA Education Series, Washington, D.C., 1994.

[3] Pagan, D., Molton, P., and Delery, J., "Basic Experiment on a Supersonic Vortex Flow Around a Missile Body," *Journal of Spacecraft and Rockets*, Vol. 29, No. 3, May 1992, pp. 373–378.

[4] Moore, F. G. and Hymer, T. C., "Semiempirical Prediction of Pitch Damping Moments for Configurations with Flares," *Journal of Spacecraft and Rockets*, Vol. 38, No. 2, March 2001, pp. 50–58.

[5] Sigal, A., "Methods of Analysis and Experiments for Missiles with Noncircular Fuselages," *Tactical Missile Aerodynamics, Prediction Methodology*, edited by M. R. Mendenhall, AIAA, 2nd ed., 1992.

[6] Kontis, K., Qin, N., and Stollery, J. L., "Computational and Experimental Investigation of Hypersonic Performance of a Lifting Elliptic Cone With and Without Strakes," AIAA Paper 97–2252, 1997.

[7] Grasso, F. and Iaccarino, G., "Influence of Crossflow and Turbulence on Vortex Flow Around a Supersonic Missile," *Journal of Spacecraft and Rockets*, Vol. 35, No. 1, Jan.-Feb. 1998, pp. 37–45.

[8] Shereda, R. E., Amidon, P. F., and Dahlem, V. I., "Wind-Tunnel Tests of Elliptical Missile Body Configurations at Mach Numbers 0.4 to 5.0," AFWAL-TR 87-3086, Dec. 1987.

[9] Shepherd, P. A. and Tod, J. R., "Development and Application of a Weapons Multiblock Suite," AGARD CP-473, May 1988, Presented at Symposium on Fluid Dynamics, Lisbon, Portugal.

[10] Edwards, J. A. and Roper, J. J., "A Computational Assessment of Static and Dynamic Coefficients for the H3 Hypervelocity Projectile," AIAA Paper 97–0640, Jan. 1997.

[11] Pesek, T. W., Bertin, J. J., Forsythe, J. R., Pluntze, S. C., Schuricht, P. H., and Abate, G., "Supersonic Flowfield for a Slender, Power-Law Elliptic-Section (PLES) Projectile," AIAA Paper 00–0120, Jan. 2000.

[12] Schuricht, P. H., Forsythe, J. R., Bertin, J. J., , and Abate, G. L., "Comparison Between Measurements and Computations for Power-Law Elliptic Section Bodies," AIAA Paper 00–2553, 2000.

[13] Grismer, M. J., Strang, W. Z., Tomaro, R. F., and Witzemman, F. C., "Cobalt: A Parallel, Implicit, Unstructured Euler/Navier- Stokes Solver," *Advances in Engineering Software*, Vol. 29, No. 3-6, 1998, pp. 365–373.

[14] Fournier, E. Y., "Testing of the USAFA H3 Model in the DREV TriSonic Wind Tunnel," DREV-TN 2000-064, 2000.

[15] Spalart, P. R. and Allmaras, S. R., "A One-EquationTurbulence Model for Aerodynamic Flows," AIAA Paper 92–0439, Jan. 1992.

[16] Baldwin, B. S. and Barth, T. J., "A One-Equation Turbulence Transport Model for High Reynolds Number Wall-Bounded Flows," NASA-TM 102847, Aug. 1990.

[17] Kennon, S. R., Meyering, J. M., Berry, C. W., and Oden, J. T., "Geometry Based Delaunay Tetrahedralization and Mesh Movement Strategies for Multi-Body CFD," AIAA Paper 92–4575, 1992.

[18] Urena, E. J. and Massett, A. P., "Shock Wave Analysis for a Power Law Elliptic (PLES) Section Configuration," Usafa project report for ae 471, 1999.